# Machine learning-based multi-objective optimization for efficient identification of crystal plasticity model parameters

Khem Veasna<sup>a</sup>, Zhangxi Feng<sup>b</sup>, Qi Zhang<sup>a,\*</sup>, and Marko Knezevic<sup>b,\*</sup>

 $^{\rm a}Department$  of Mathematics and Statistics, University of New Hampshire, Durham, NH 03824, USA

#### Abstract

A set of constitutive model parameters along with crystallography governs the activation of deformation mechanisms in crystal plasticity. The constitutive parameters are typically established by fitting of mechanical data, while microstructural data is used for verification. This paper develops a Pareto-based multi-objective machine learning methodology for efficient identification of crystal plasticity constitutive parameters. Specifically, the methodology relays on a Gaussian processes-based surrogate model to limit the number of calls to a given crystal plasticity model, and, consequently, to increase the computational efficiency. The constitutive parameters pertaining to an Elasto-Plastic Self-Consistent (EPSC) crystal plasticity model including a dislocation density-based hardening law, a backstress law, and a phase transformations law are identified for two materials, a dual phase (DP) steel, DP780, subjected to load reversals and a stainless steel (SS), 316L, subjected to strain rate and temperature sensitive deformation. The latter material undergoes plasticity-induced martensitic phase transformations. The optimization objectives were the quasi static flow stress data for the DP steel case study, while a set of strain-rate and temperature sensitive flow stress and phase volume fraction data for the SS case study. The procedure and results for the two case studies are presented and discussed illustrating advantages and versatility of the developed methodology. In particular, the efficiency of the developed methodology over an existing genetic algorithm methodology is discussed. Additionally, the parameters identified for the SS case study were utilized to simulate three biaxial tensile loading paths using a finite element implementation of EPSC for further verification.

 ${\it Keywords}$ — Crystal plasticity; Machine learning; Numerical algorithms; Parameter identification

<sup>&</sup>lt;sup>b</sup>Department of Mechanical Engineering, University of New Hampshire, Durham, NH 03824, USA

 $<sup>^*</sup> Corresponding \ authors: \ Qi.Zhang 2@unh.edu, \ Marko.Knezevic @unh.edu$ 

# 1 Introduction

To attain a solution for the balance of linear momentum governing equation under the action of applied deformation in continuum mechanics, a constitutive law describing the material strength is needed. The sought solution in terms of stress and strain fields is commonly obtained numerically using methods such as the self-consistent (SC) scheme [1] or the finite element (FE) method [2]. Accuracy of the sought solution is dependent on the accuracy and flexibility of a selected constitutive law. Constitutive laws based on crystal plasticity theory are known as more accurate than phenomenological laws because they are based on crystallography of deformation mechanisms and they account for microstructure and texture evolution during deformation. These laws are multi-scale in nature because they link the constituent grain level deformation response to the that of a polycrystalline aggregate. Although known as more accurate, these models are yet to be adopted by practical users because of the prohibitive computational effort and time involved in such simulations and because specialized expertise is required for model parameters identification for successful simulations.

With the appropriate model parameters identification, crystal plasticity models (CPMs) can simulate monotonic or strain-path change deformations while accounting for texture, dislocation density, and phase evolution [3, 4, 5, 6], reveal underlying deformation mechanisms [7, 8, 9, 10], and define new experimental procedures for understanding materials [11, 12, 13]. CPMs are being constrained with rich data including the diffraction techniques which provide robust datasets [14, 15, 16, 17]. No matter how complex the data is, a particular parameter is usually constrained with the specific portion of the data. Moreover, essential in the identification process is to ensure that the identified parameters are physical, else the model will not be able to extrapolate the predictive characteristics. In summary, effective crystal plasticity simulations, extrapolating the predictive capabilities to high strains, high strain-rates, complex geometries [18, 19, 20], and maximizing learning and experimental impact [21, 22] are only possible with appropriately constrained model parameters.

CPMs have traditionally been calibrated by changing parameters manually to fit a representative dataset. Such process requires expertise and significant time. Identification of CPM parameters from mechanical data using automated optimization schemes [23] and multivariant analysis [18] have been attempted in the past. A methodology optimizing the crystal elastic moduli and plasticity parameters were implemented recently [24, 25] by matching discrete spherical harmonic modes of lattice strain pole figures from simulated and measured high energy x-ray diffraction data. Bandyopadhyay et al. [26] developed an algorithm to calibrate CPM parameters by utilizing GA to estimate the uncertainty quantification in the output of the models. Recently, Proper Generalized Decomposition (PGD) has been used for material model calibration [27]. Pareto-based multi-objective optimization schemes have also been used to optimize parameters of damage models such as the Gurson-Tvergaard-Needleman model [28, 29, 30].

A recent work reported in [31] utilized an advanced methodology involving an expensive function optimization strategy for constructing a surrogate model. Searching a response surface with a genetic algorithm (GA) along with updating the response surface, parameters were identified using mechanical data with limited number of calls on the compiled executable of the model. The primary limitation of the procedure reported in [31] was relying only on the mechanical data. Additionally, the procedure in [31] approximated the response surface using second-order polynomial with up to four-way interactions, preventing the use of material models with more than just a few parameters to fit. A more recent multi-objective GA (MGA) procedure reported in [32] considered not only mechanical data but also microstructural evolution data to constrain the models being fit more rigorously. Incorporating more than mechanical data as objectives was found es-

sential in improving the parameter identification. However, the MGA procedure in [32] was computationally demanding because of a large number of model calls and also required advanced computational platforms [32]. The aim of the present work is to combine advantages of these prior works [31, 32, 33], and to take a significant step further. This work deploys a budgeted sequential infilling algorithm that allows a user to set a fixed budget, where a budget is a number that caps the amount of runs of an expensive black-box function and infilling is a procedure to find new candidate points. The infill points are sets of parameters added as new potential solutions. To this end, the novel procedure advances [32] by incorporating a machine learning based surrogate model to limit calls (i.e., assign a fixed budget) to the material model and, consequently, to increase computational efficiency.

The development and applications of machine learning tools in various aspects of material science research have recently been reviewed in [34]. Advantages of integrating machine learning tools and CPMs are being recognized in creating efficient constitutive models for polycrystalline simulations and integrated computational materials engineering applications [35, 36, 37]. In particular, polynomial approximation of response surfaces and canonical correlation analyses were used in sensitivity and parameter identification studies [31, 18]. Gaussian process (GP) models, also known as Kriging, have been used in constructing structure-property linkages [38], more recently, in fluid dynamics simulation [39], and in linking crystal plasticity results to part scale simulations [33]. Barton et al. used a metric-tree database for course-scale queries, which explores a pre-determined region, and Kriging as an adaptive scheme to search for optimal points under some threshold [33]. In our work, Kriging models are fitted to the responses where the inputs are from Latin hypercube sampling and the subsequent infillings. In a sense, these are like course-scale queries. The goal of our sequential search via GP-based infilling is to hone in on optimal points under a budget restriction. The present work utilizes GP models to develop a Pareto-based multi-objective machine learning methodology for efficient identification of crystal plasticity constitutive parameters. To this end, a budgeted sequential infilling procedure is developed based on GP surrogate models and shown that it is able to identify optimal model parameters, while significantly reducing the amount of computation time relative to GA-based procedures. The novel procedure and results for several case studies are presented and discussed in this paper illustrating advantages, versatility, and computational efficiency.

# 2 Methods

The goal of optimization is improvement of given objectives in each iteration. Complex systems with multiple objectives can have multiple optima; one such system is the identification of model parameters in CPMs. Selecting any one of the calculated optima can be an acceptable solution to reproduce the data. However, the identified parameters must be in the range of their physical values. Therefore, there is an extra step upon completing the optimization iterations, which is selecting a final optimum set of model parameters from evaluated optima.

The multi-objective optimization formulation is:

Minimize 
$$y(x) = \{y^{(1)}(x), y^{(2)}(x), \dots, y^{(q)}(x)\}^T,$$
 (1)

where  $x \in \mathcal{D}$  and  $y^{(j)}(x)$  is the j-th objective function to be minimized.  $\mathcal{D}$  is the space of the vector x representing a set of parameter.

This work deploys a budgeted sequential infilling algorithm that allows a user to set a fixed budget. The budget (the number of simulations runs) is a number that caps the amount of runs of an expensive black-box function. Suppose that for each simulation run there are N objectives. Since each objective requires a

run of an executable, the result is B\*N runs of the executable. In our work, y(x) is the black-box function consisting of objectives calculated based on a selected CPM. A sequential search of the parameter space finds new points (called infill points) for objective/fitness function evaluations—the error between the black-box function and its true value (experimental measurements)—and updates the Gaussian process (GP) surrogate model, accordingly, as explained next. While the GP surrogate model establishes suitable infill points, the objectives are exclusively evaluated upon running the selected CPM.

#### 2.1 Gaussian processes

GP or Kriging originated as a geostatistical interpolation method, which was extended to the design and analysis of computer experiments [40]. A GP is a collection of random variables where any finite number of them have a joint Gaussian or multivariate normal distribution [41]. It is a general approximation method for an unknown deterministic black-box function f(x). The general model setup for GP is:

$$f(x) = \nu(x) + Z(x), \tag{2}$$

where  $x \in \mathcal{D}$ ,  $\nu : x \in \mathcal{D} \to \nu(x) \in \mathbb{R}$  is a deterministic trend and Z(x) is a centered-stationary random GP with zero mean and a stationary covariance kernel (or covariance function) expressed as:

$$K(\boldsymbol{x}, \boldsymbol{x}^*) = Cov(Z(\boldsymbol{x}), Z(\boldsymbol{x}^*)) = \sigma^2 R(\boldsymbol{x}, \boldsymbol{x}^*, \boldsymbol{\theta}),$$
(3)

where  $\boldsymbol{x}, \boldsymbol{x}^* \in \mathcal{D}$ ,  $\sigma^2$  is the variance parameter, R is the correlation function, and  $\boldsymbol{\theta}$  is a vector of characteristic length-scales consisting of hyperparameters [39]. In this work, the Matern 5/2 kernel is used to get the correlation function:

$$R(\boldsymbol{x}, \boldsymbol{x}^*) = \prod_{i=1}^{d} (1 + \sqrt{5}\theta_i m_i + \frac{5}{3}\theta_i^2 m_i^2) exp(-\sqrt{5}\theta_i m_i) , \qquad (4)$$

where  $x_i$  and  $x_i^*$  are the i-th components of  $\boldsymbol{x}$  and  $\boldsymbol{x}^*$ , respectively,  $m_i = |x_i - x_i^*|$ , and d is the dimension of  $\mathcal{D}$ .

An initial construction of the GP model is done through a design of experiments (DOE) methodology. Latin hypercube sampling (LHS) is a technique used in the DOE as a space-filling design for this work. Let a collection of n (typically,  $n=10 \times$  the number of parameters) observations from LHS be  $X_n = \{x_1, ..., x_n\} \subset \mathcal{D}$ , and let the data be  $D_n = (X_n, f(X_n))$ . The n observations is modeled as having a multivariate normal (MVN) distribution since there is a finite number of realizations of the GP—i.e., evaluations of f(X). The characteristics of the observations are completely described by their n-vector mean,  $\mu_n = (\mu(x_1), ..., \mu(x_n))$  (where  $\mu(x) = \mathbb{E}[f(x)] = \mathbb{E}[\nu(x)]$ ), and  $n \times n$  covariance matrix,  $\Sigma_n = K(X_n, X_n)$ . The conditional distribution  $f(X)|D_n$  (or the posterior)—which, again, is a multivariate normal distribution—explains what random function realizations could have generated the observed values. Interpolation of f(x) is done by sampling from the posterior distribution. For example, assume the mean function is zero and let  $X_m \subset \mathcal{D}$  be m new observations, then we have the following:

$$f(\mathbf{X}_m)|D_n \sim \mathcal{N}(\boldsymbol{\mu}^*, \boldsymbol{\Sigma}^*),$$
 (5)

where  $\boldsymbol{\mu}^* = K(\boldsymbol{X_m}, \boldsymbol{X_n}) \boldsymbol{\Sigma}_n^{-1} f(\boldsymbol{X_n})$ , and  $\boldsymbol{\Sigma}^* = K(\boldsymbol{X_m}, \boldsymbol{X_m}) - K(\boldsymbol{X_m}, \boldsymbol{X_n}) \boldsymbol{\Sigma}_n^{-1} K(\boldsymbol{X_m}, \boldsymbol{X_n})^T$ .

The procedure for sequential searching of infill points is called the infilling criterion, as described next. New infill points will be considered until the budget is exhausted.

## 2.2 Infilling criterion

The infilling criterion such as the efficient global optimization (EGO) algorithm of Jones et al. [42] is based on expected improvement (EI). Let f(x) be GP for the mono-objective case, and suppose we have n GP outputs  $y_1, \ldots, y_n$  at our inputs  $x_1, \ldots, x_n$ , then the EI is defined as:

$$EI(\boldsymbol{x}) = \mathbb{E}\left[\max\left(0, \min_{1 \le i \le n}(y_i - f(\boldsymbol{x}))\right) \mid f(\boldsymbol{x}_1) = y_1, \dots, f(\boldsymbol{x}_n) = y_n\right].$$
(6)

While for the multi-objective case, scalarization—i.e., mapping a vector of objectives to a scalar—can be invoked to utilize EI, it may not work well without additional assumptions [43]. Techniques such as those proposed by Jones et al. [42] improve on this by estimating the improvement brought on by a potential solution (from the surrogate model) to the set of non-dominated points, as elaborated in the next section.

In the multi-objective settings, infill points (a set of parameters) are chosen based on a set of GP models as described in the prior section. The goal is to identify infill points yielding better objectives/fitness, i.e., smaller error. For the multi-objective case, there are more than one GP model—one for each objective. It should be noted that it is possible to use even a more complex multivariate GP (i.e., CoKriging). However, there is little to gain with the additional complexity based on empirical data as elaborated in [44, 45]. The set of optimal solutions in the multi-objective case is called the Pareto optimal points—this forms the Pareto front.

The S-metric Selection Efficient Global Optimization (SMS-EGO) approach is an improvement function which computes the hypervolume added to the current Pareto front by the lower confidence bound of the prediction at x [46]. The S-metric or hypervolume indicator is a method to evaluate how close a point set is to the Pareto front. For a given reference point, r, the hypervolume indicator of a set S is the volume of all points which weakly-dominate r, and we use H(S) to denote it [47]. The reference point can be determined from the evaluations of the black-box functions of the initial design—i.e., the maximum value of each objective.

SMS-EGO uses the surrogate GP models to search for new candidate points. The best candidates are selected by maximizing the improvement of hypervolume indicator of the Pareto set after being combined with the potential solution. In general, hypervolume contribution of a set X to S—i.e., the improvement in hypervolume indicator by incorporating X—is defined as [47]:

$$H(X,S) = H(X \cup S) - H(S/X) \tag{7}$$

The goal is to find the set of non-dominated or Pareto-optimal points—i.e.

$$\{oldsymbol{x}_1^*,...,oldsymbol{x}_m^*\}\subset\mathcal{D},$$

where m is the number of points in the Pareto set (which varies) and none of these points is superior to any other points in this set in terms of all objectives. With the new potential solution, the black-box function (CPM) is evaluated, and the GP models are also updated by adding new points. This procedure repeats until the budget is exhausted.

Figure 1 shows a flowchart that describes the infilling algorithm:

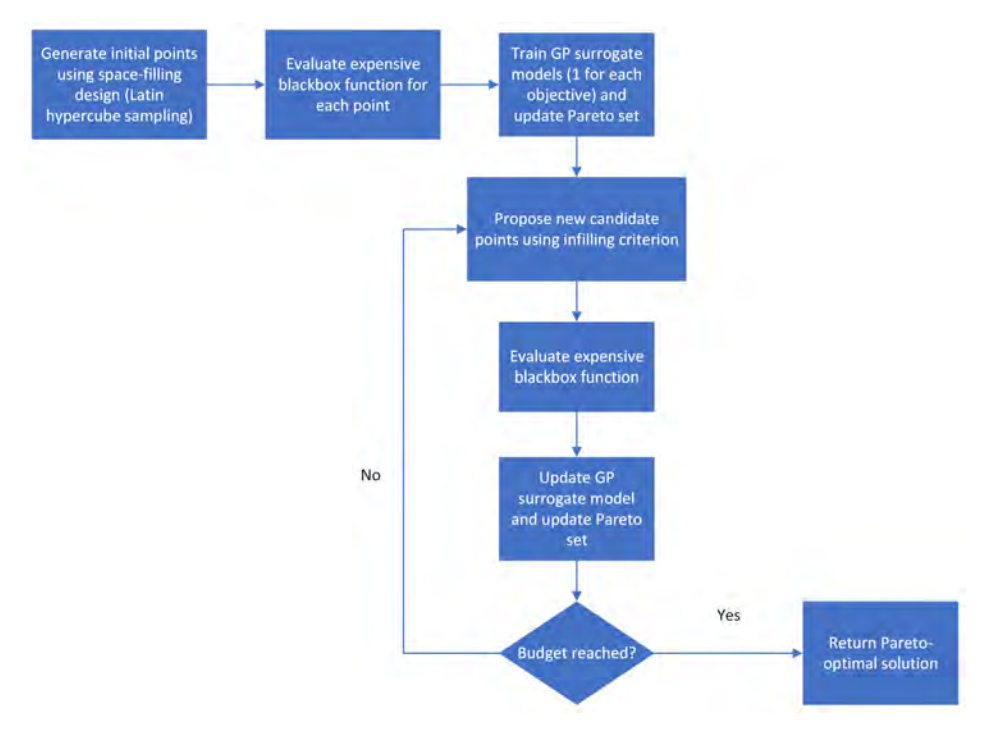


Figure 1: Flowchart showing the budgeted sequential infilling algorithm.

# 2.3 From Genetic Algorithm to sequential infilling algorithm for crystal plasticity modeling

In an MGA-based procedure, a compiled CPM is run for each objective per population to compute the simulated results given a set of parameters for each generation. The algorithm stops once the maximum number of generations is reached or when there are no appreciable improvements in comparison with the previous generation of parameters, which is usually controlled via a parameter [43].

GA generates an initial population in the first generation randomly and approaches better solutions over generations. The new solutions are generated via genetic mutations and breeding algorithms which mimic the process of natural selection.

Since a CPM usually takes a few minutes to run, the run-time adds up quickly. For each population in the generation, the GA has to run the model once for each independent case. Some unreasonable combinations of parameters may also cause the model to fail to converge and hang the process indefinitely until it is automatically terminated by the batch process when a maximum time is reached. Fortunately, the model can be executed independently on separate CPUs allowing for parallelization to speed up the optimization process.

The number of runs of CPM for GA depends on the number of generations, the populations size, and the size of an individual (number of parameters). The number of runs of CPM for the infilling algorithm is the size of the initial design plus the budget size, which is much less than with GA, as will be shown later. While the number of simulation runs needed may be high, one of the main advantages of GA is that it scales well with the use of parallelism. It is also known to be a robust method for a wide variety of problems [48].

For CPM, a budgeted sequential infilling algorithm can identify suitable parameters with a small number of simulations, as will be shown. There are two major differences between the two methodologies. GA runs CPM for all candidate points, and select the next generation from them. In contrast, our methodology runs CPM only for the selected infill points. The other difference is the stopping criteria. Our methodology is based on a budget; GA's stopping criteria can be based on convergence (e.g., no improvements in the population for some number of iterations), hard stop after some number of generations, or the objective func-

tion satisfies some tolerance level. The latter was used in the previous work [32]. It will be shown later that we were able to identify suitable CPM parameters with a small number of simulation runs with our methodology compared to GA. In theory, computing the variance-covariance matrix for Kriging when the training set is large can potentially become a computational bottleneck. But it is not an issue in our study. The advantage of using a stopping criteria such as with an objective function that satisfies some tolerance level, is that it allows the user to specify how well of a fit they want, at the expense of high number of simulation runs. In our methodology, a budget size is the only constraint. A larger budget will yield more accurate solution.

# 2.4 Summary of the CPM objectives

This work combines the GP-based surrogate model and multi-objective optimization to efficiently identify the constitutive parameters of an Elasto-Plastic Self-Consistent (EPSC) CPM. The EPSC model embeds a dislocation density-based hardening law along with a backstress law and a martensitic phase transformations law to model mechanical behaviors of steel alloys. The formulation is summarized in appendix A.

The optimization scheme was first applied to search a parameter space and identify a set of optimized Pareto parameters for 1.4 mm sheets of a dual phase (DP) advanced high strength steel (AHSS), DP780 [49]. The material contains 34% of martensite, while the other phase present in the microstructure is ferrite (66%). The steel had a typical orthotropic rolled initial texture, which was represented with 500 weighted orientations [50, 51, 52]. Appendix B shows the initial texture. The steel was tested experimentally in cyclic tension-compression strain paths under a nominal strain-rate of  $5e^{-4}s^{-1}$  at room temperature [49]. In addition to the hardening law parameters for slip, the complete list of parameters to optimize includes those of the backstress law in order to capture the load-reversal deformation behavior of the steel. The objectives were the experimental flow stress data recorded during the cyclic testing. In the model, we compute the objective as the root-mean-square error (RMSE) between the simulated and experimental curves.

The parameters to be identified for slip are the initial slip resistance,  $\tau_0^{\alpha}$ , trapping rate coefficient,  $\kappa_1^{\alpha}$ , drag stress,  $D^{\alpha}$ , and activation barrier for de-pinning,  $g^{\alpha}$ , per phase (ferrite and  $\alpha'$ -martensite). The superscript  $\alpha$  enumerates slip modes/families, while s enumerates the individual slip systems per mode. The slip modes available to accommodate plastic strains in the body-centered cubic (BCC) steel phases of ferrite and  $\alpha'$ -martensite are  $\alpha=1$  for  $\{110\}$  and  $\alpha=2$  for  $\{112\}$ . The parameters are assumed identical for both slip modes. While  $\tau_0$  influences the initial yielding,  $\kappa_1^{\alpha}$  governs primarily the initial hardening rate and  $D^{\alpha}$  and  $g^{\alpha}$  govern the subsequent hardening rates. Additionally, the initial state of forest dislocation density influencing the initial yielding of the steel,  $\rho_{0,for}^{s}$ , was allowed to vary for each phase. Simultaneously with the hardening law parameters, the backstress law parameters for ferrite need fitting. These include the saturation for backstress,  $\tau_{bs}^{sat}$ , asymmetry factor,  $A_{bs}$ , and coefficients  $\nu$  and  $\gamma_b$ . These parameters are fit to obtain the unloading and asymmetric yield at load reversals.

The optimization scheme was subsequently applied to identify parameters for modeling of 1.2 mm sheets of SS316L austenitic steel undergoing strain-induced martensitic phase transformations. The slip mode available to accommodate plastic strains in the face-centered cubic (FCC) austenite phase is  $\{110\}$  octahedral slip, while that of the hexagonal close-packed (HCP)  $\varepsilon$ -martensite phase is  $\{01\bar{1}1\}$  pyramidal slip. The  $\alpha'$ -martensite phase is BCC, whose slip modes were already defined. The initial material also had a rolled texture [53, 54], which was represented with 500 weighted orientations for simulations. Appendix B shows the initial texture. The experiments to acquire mechanical and phase fractions data

included uniaxial tension in the rolling direction under four strain rates at a constant temperature of 20 °C and four temperatures at a quasi-static strain-rate of  $0.001 \ s^{-1}$ . The details pertaining to preserving the isothermal condition during the tests can be found in [53]. The recorded flow stress curves and phase fractions were used as the objectives. The response as well as the transformed martensite volume fractions was temperature and strain rate sensitive. Therefore, the initial slip resistance for SS316L is formulated to be strain rate and temperature dependent, as described in the appendix. Instead of the backstress law parameters, the phase transformation law parameters were fit for SS316L. These included a slope for the stacking fault energy,  $m_{SFE}$ , an intercept for the stacking fault energy,  $C_{SFE}$ , a slope for the triaxiality effect on phase transformations,  $\kappa_{\beta}$ , and an intercept for the triaxiality effect,  $\beta_0$ . The initial forest dislocation density was fixed to  $\rho_{0,for}^s$ =3e<sup>11</sup> for austenite, while the transformed phases inherit the value from parent phase upon nucleation. The optimized parameters for SS316L were then used to simulate three biaxial tensile loading paths performed on cruciform specimens. The three paths defined in terms of rolling direction (RD) to transverse direction (TD) displacement ratios are: 4:4, 2:4, and 0:4, following the experiments reported

Table 1 summarizes the data to fit along with the objectives used in the optimization to identify model parameters per material. Table 2 and Table 3 define the EPSC parameters being optimized and their lower and upper bounds that define the parameter space,  $\mathcal{D}$ . The upper and lower bounds are chosen to be the parameters' expected maximum and minimum possible values based on understanding of the mechanical data, calibration experience using prior manual methods, and literature. Next section describes a sequential infilling pipeline (or application) streamlining the process of using the budgeted sequential infilling algorithm for CPM while highlighting robustness of the system that is configurable and easy to modify.

Table 1: Summary of data to fit, labeling of the data, and objectives used in the optimization scheme to identify model parameters for DP780 and SS316L. The DP780 steel was tested experimentally by applying cyclic tension-compression strain paths under a nominal strain-rate of  $5e^{-4}s^{-1}$  at room temperature. The stress-strain objective implies about 200 discrete points for each simple tension curve and about 1000 discrete points for each cyclic curve. The phase fraction data contains only 3 data points, but these are critical objectives for fitting the phase transformation parameters.

Case ID	Material	Objective(s)	Test conditions
1	DP780	Stress strain	Compression to 0.1 strain
2	DP780	Stress strain	Strain path: 0.01 prestrain, unload, then pull to fracture
3	DP780	Stress strain	Strain path: 0.02 prestrain, unload, then pull to fracture
4	DP780	Stress strain	Strain path: 0.05 prestrain, unload, then pull to fracture
5	DP780	Stress strain	Strain path: 0.1 prestrain, unload, then pull to fracture
6	DP780	Stress strain	Strain path: $0 \rightarrow 0.02 \rightarrow 0.02 \rightarrow 0.02 \rightarrow 0.04 \rightarrow 0 \rightarrow 0.06$ up to fracture with the strain amplitude of 0.04 and the mean strain increase of 0.02 per cycle.
7	DP780	Stress strain	Strain path: $0 \rightarrow 0.02 \rightarrow 0.04$ $\rightarrow 0.02 \rightarrow 0.06 \dots$ up to fracture with the strain amplitude of 0.02 and the mean strain increase of 0.02 per cycle.
8	DP780	Stress strain	Strain path: $0 \rightarrow 0.02 \rightarrow 0.02 \rightarrow 0.02 \rightarrow 0.03 \rightarrow 0.01 \rightarrow 0.04 \dots$ up to fracture with the strain amplitude of 0.04 and the mean strain increase of 0.01 per cycle.
9	DP780	Stress strain	Strain path: $0 \rightarrow 0.02 \rightarrow 0.02 \rightarrow 0.02 \rightarrow 0.04 \rightarrow 0.04 \rightarrow 0.06 \dots$ up to fracture.
AA	SS316L	Stress strain	$\dot{\varepsilon}_1 = 1e^{-3}s^{-1}, T_4 = 20  ^{\circ}\text{C}$
ВВ	SS316L	Stress strain	$\dot{\varepsilon}_2 = 1e^{-4}s^{-1}, T_4 = 20 ^{\circ}\text{C}$
CC	SS316L	Stress strain	$\dot{\varepsilon}_3 = 1e^{-2}s^{-1}, T_4 = 20  ^{\circ}\text{C}$
DD	SS316L	Stress strain	$\dot{\varepsilon}_4 = 5e^{-3}s^{-1}, T_4 = 20  ^{\circ}\text{C}$
EE	SS316L	Stress strain Phase fractions	$\dot{\varepsilon}_1 = 1e^{-3}s^{-1}, T_1 = -15 ^{\circ}\text{C}$
FF	SS316L	Stress strain Phase fractions	$\dot{\varepsilon}_1 = 1e^{-3}s^{-1}, T_2 = 0  ^{\circ}\text{C}$
GG	SS316L	Stress strain	$\dot{\varepsilon}_1 = 1e^{-3}s^{-1}, T_3 = 10  ^{\circ}\text{C}$

Table 2: Parameters to optimize for DP780 within their upper and lower fitting bounds. The superscripts fer and mart denote the parameters for ferrite and  $\alpha'$ martensite phases, respectively. The backstress parameters are for ferrite.

DP780	Bounds	Description	
$\kappa_1^{\alpha,fer}[m^{-1}]$	[1e+8, 1e+9]	Rate of dislocation generation	
$\kappa_1^{\alpha,mart}[m^{-1}]$	[1e+8, 1e+9]	trate of dislocation generation	
$\tau_0^{\alpha,fer}[MPa]$	[10, 100]	Initial slip resistance	
$\tau_0^{\alpha,mart}[MPa]$	[10, 1000]	imital sup resistance	
$\rho_{0,for}^{s,fer}[m^{-2}]$	[1e+10, 1e+12]	Initial forest dislocation density	
$\rho_{0,for}^{s,mart}[m^{-2}]$	[1e+10, 1e+12]		
$g^{\alpha,fer}$	[0.001,  0.02]	Activation energy	
$g^{lpha,mart}$	[0.01, 0.2]	Activation energy	
$\overline{D^{\alpha,fer}[MPa]}$	[100, 1000]	Drag stress	
$D^{\alpha,mart}[MPa]$	[100, 1000]		
$\tau_{bs}^{sat}[MPa]$	[50, 150]	Saturation value	
ν	[50, 150]	Forward shear parameter	
$\gamma_b$	[0.001,  0.01]	Reverse shear parameter	
$A_{bs}$	[1, 5]	Asymmetric evolution parameter	

Table 3: Parameters to optimize for SS316L within their upper and lower fitting bounds. The superscripts aus and mart denote austenite and  $\alpha'$ -martensite phases, respectively.

SS3416L	Bounds	Description	
$\overline{\kappa_1^{\alpha,aus}[m^{-1}]}$	[1e+8, 2e+8]	Rate of dislocation generation	
$\kappa_1^{\alpha,mart}[m^{-1}]$	[1e+8, 3e+8]	trate of dislocation generation	
$g^{\alpha,aus}$	[0.1, 0.25]	Activation energy	
$g^{\alpha,mart}$	[0.1, 0.4]	receivation energy	
$D^{\alpha,aus}[MPa]$	[100, 200]	Drag stress	
$D^{\alpha,mart}[MPa]$	[200, 400]	Drag stress	
$\tau_{0,a}^{\alpha,aus}[MPa]$	[200, 400]	Initial slip resistance coefficient a	
$\tau_{0,a}^{\alpha,mart}[MPa]$	[100, 500]	initial sup resistance coefficient a	
$ au_{0,b}^{lpha,aus}$	[0.01,  0.08]	Initial slip resistance strain-rate	
$ au_{0,b}^{lpha,mart}$	[0, 0]	coefficient, b	
$ au_{0,c}^{lpha,aus}[K]$	[200, 400]	Initial slip resistance temperature	
$\tau_{0,c}^{\alpha,aus}[K]$	[1e+6, 1e+6]	coefficient, c	
$m_{SFE}[\frac{mJ}{Km^{-2}}]$	[0.01, 0.5]	Stacking fault energy slope	
$C_{SFE}[\frac{mJ}{m^{-2}}]$	[5, 15]	Stacking fault energy intercept	
$\kappa_{eta}$	[0.1, 0.8]	Triaxiality slope	
$eta_0$	[0.1, 0.5]	Triaxiality intercept	

#### 2.5 Sequential infilling pipeline for EPSC

The pipeline was designed specifically for the purpose of identifying EPSC parameters, but it can be adapted for other applications. It was developed using Python and R, without any dependency on commercial applications like Matlab®; GPareto is used as a dependency for multi-objective optimization[44] and DiceDesign is used as a dependency for Latin hypercube sampling [56]. It is called a pipeline because it streamlines the process of setting up an experiment, running the budgeted sequential infilling algorithm, and saving the intermediate data. Since the simulation calls are expensive, the parameters and results of the simulation calls are saved so they can be reused or checked for issues.

Parallelization is used whenever possible to speed up the runs. For sequential infilling, the parallelization distributes the simulation runs across available cores. In the initial design phase where sampling is done via the space filling design, this can be processed asynchronously. Therefore, multiple nodes can be used to process data points from the initial design, such as within a cluster, to speed up the process. For example, with 9 cases or objectives, the initial training of the models using data points from Latin hypercube sampling is done in parallel —i.e., for 190 data points, all 190 points and the evaluation of the material models for all 9 are done in parallel. With sequential infilling, the candidate points are produced one at a time. Therefore, for each point, the material models for all 9 are executed in parallel.

In addition, the application has controls in place to terminate EPSC processes when they run for too long. Figure 2 shows the design of the application.

It is possible to use the pipeline on one node because the number of simulation runs is a fraction of those needed in a GA-based methodology. With GA, it would take many days to run on one node, as will be discussed in the next section.

Figure 3 shows a high-level flowchart of the application integrated with EPSC. While EPSC is selected as a CPM for the work presented here, the figure identifies several other CPMs including Taylor-type models [57, 58, 59], Taylor-type models embedded in crystal plasticity finite elements (T-CPFE) [60, 61, 62, 63, 64], self-consistent (SC) models EPSC/VPSC [65, 66], FE versions of the SC models [33, 67, 68], and efficient versions of the elasto-visco-plastic fast Fourier transform-based (EVPFFT) models [69, 70, 71, 72], which are also suitable for computationally less efficient identification of CPM parameters. However, the runtime would vary depending on the selected model. The optimization involving high fidelity models such as full-field EVPFFT/CPFE would be more computationally demanding. The present work selected a lower fidelity mean-field model to demonstrate the optimization methodology due to the costly runtime of those higher fidelity models.

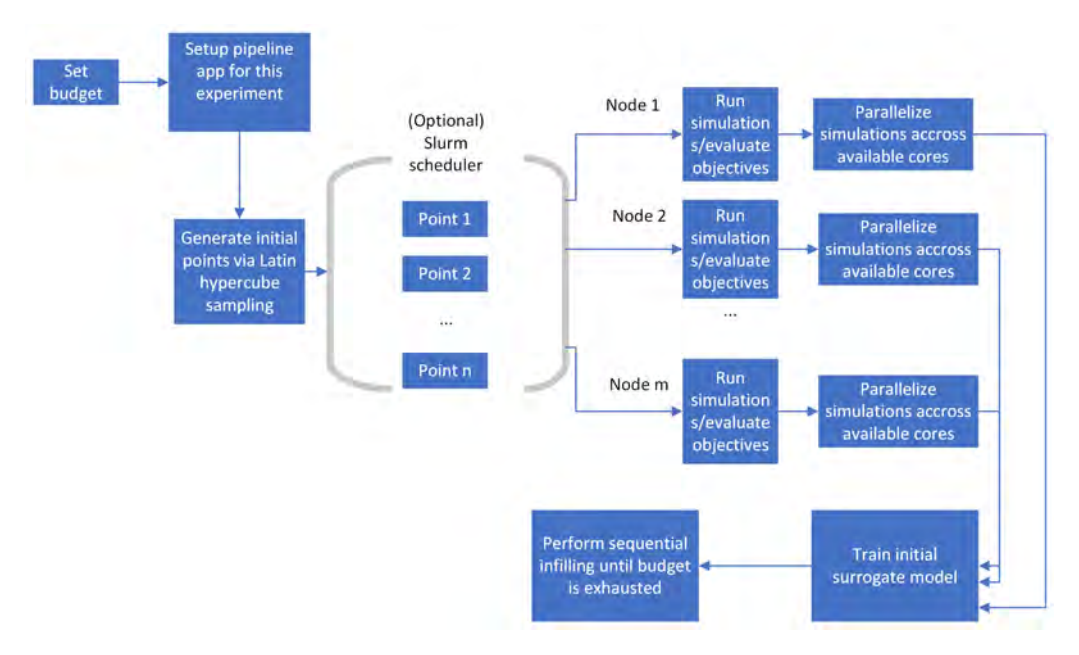


Figure 2: Flowchart showing architecture of the pipeline application.

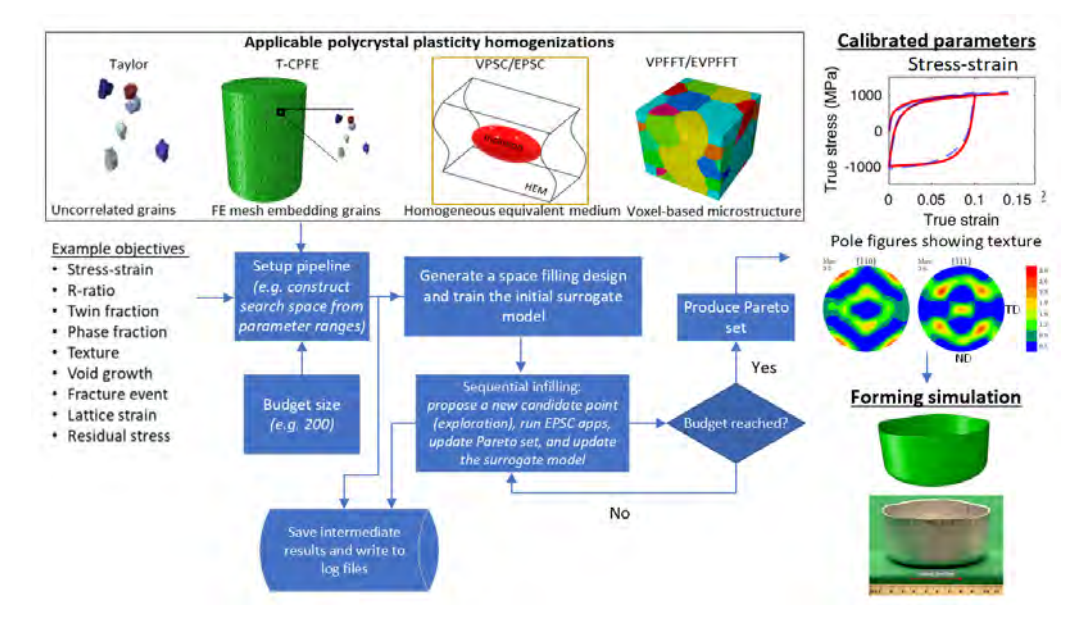


Figure 3: Flowchart showing the pipeline interacting with EPSC.

# 3 Results and discussion

The EPSC was calibrated for two steels using the above described sequential infilling pipeline.

# 3.1 Application to DP780

The prior work relied on the GA-based procedure with an initial population of 520 for 51 generations and 9 loading cases resulting in 238,680 simulations calls—a little over 3.6 days on 4 nodes with 32 cores per node (or 128 in total) on a cluster [32]. With a budget of 150, 14 parameters and 9 strain paths, the amount of simulation calls in the present work was 2,610—around 2 days on a single node with 4 cores. Evidently, the machine learning-based multi-objective optimization developed in the present work for identification of crystal plasticity model parameters is about two orders of magnitude more efficient than the former GA-based procedure.

In multi-objective optimizations multiple Pareto optima exist. These Pareto optima are the solutions that cannot be ruled out by the Pareto method. Moreover, the optima are not necessarily equivalently suitable solutions. Further ranking of these optima is needed. In the case of DP780, the Pareto front set consisted of 40 solutions. To evaluate these solutions, RMSE of all objectives is calculated to rank the solutions in an ascending order for finally selecting the most physical solution through visual inspection. Here, we calculate the average over objectives (each objective is an RMSE between one experimental curve and corresponding simulated curve discretized into many points) to rank the solutions. Additionally, we normalize RMSE per objective to get a percent error. The ranking plots are shown in appendix C. The selected solution is not necessarily the one with the lowest average error but the most physical one and with as low as possible RMSE. After sorting the solutions based on the average error of all objectives in the ascending order, the best candidates are then visually inspected to select the most physical solution. While most of the solutions provide good fits, we chose the first sufficiently physical set that has the lowest error as a solution. The selected solution is not necessarily the one with the lowest average error. The nature of crystal plasticity model parameters is that they are not unique. Having a fully automated procedure for parameter identification is an extremely challenging task. Some human inspection must be involved based on understanding of the mechanical data, calibration experience using prior manual methods, and literature. The optimized set of parameters are shown in Table 4, and the objectives are shown in Figures 4 and 5, where Optimum 1 and Optimum 2 are two different optimal solutions chosen from a reduced Pareto front set of optima with low RMSE based on the criteria of the most physical set with lowest error. A physical set of the parameters is defined as the set providing qualitatively similar calculated curves to the measured curves in terms of yield stresses and hardening rates, expected values for some of the parameters like the initial dislocation densities or initial slip resistances, and good comparisons with available values in the literature for some parameters like in [49] for DP steels. Optimum 1 is the most physical solution, while Optimum 2 is presented to show one other solution from the set of multiple optima. While the main purpose of the DP780 steel data was to provide a direct comparison with the previous work involving the GA-based optimization (appendix D), we also run a verification case study. To this end, we adjust the optimization process to consider cases 1, 2, 3, 4, 6, 7, and 9 as objectives, while cases 5 and 8 are predictions of the optimized parameters from the other 7 cases. The obtained results were similar to those with fitting all 9 cases and, therefore, are not shown. Finally, appendix D shows comparisons between past results from the genetic algorithm optimization and current results obtained using the optimization developed in the present work.

Table 4: Two optima of EPSC model parameters for ferrite and martensite phases of DP780 steel identified using the developed Pareto-based multi-objective machine learning procedure for efficient identification of crystal plasticity model parameters. Crystal elastic constants are also necessary to run the model:  $C_{11}^f = 206$  GPa,  $C_{12}^f = 135$  GPa, and  $C_{44}^f = 117$  GPa for ferrite and  $C_{11}^m = 282$  GPa,  $C_{12}^m = 135$  GPa, and  $C_{44}^m = 117$  GPa for martensite [73, 74].

	Ferrite		Martensite	
Parameters	Optimum 1	Optimum 2	Optimum 1	Optimum 2
$\kappa_1^{\alpha}[m^{-1}]$	1.33e + 08	6.35e + 08	1.2e+08	1.71e+08
$ au_0^{lpha}[MPa]$	61.7	37.8	532	314
$\rho^s_{0,for}[m^{-2}]$	1.4e + 11	1.5e + 11	6.7e + 11	6.5e + 11
$g^{lpha}$	0.00723	0.00899	0.115	0.113
$D^{\alpha}[MPa]$	560	564	620	622
Backstress parameters for ferrite				
$\tau_{bs}^{sat}[MPa]$	54.8	135		
ν	136	88		
$\gamma_b$	0.00293	0.00472		
$A_{bs}$	3.85	2.63		

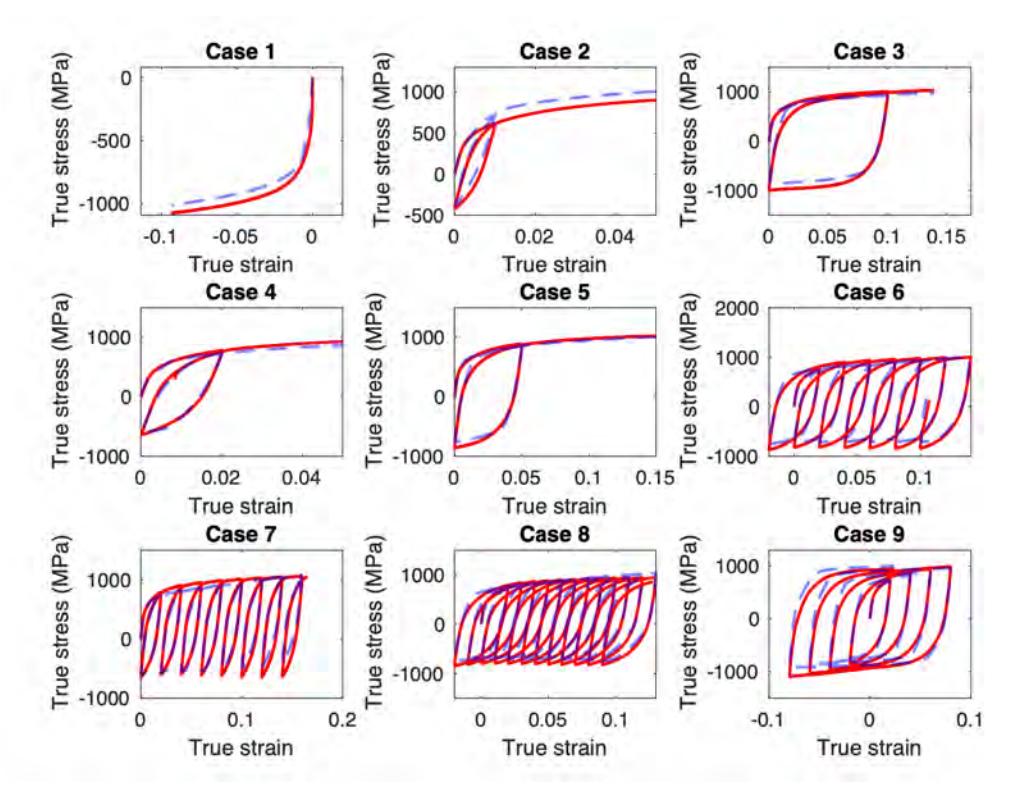


Figure 4: Comparison between experimental curves taken from [49] (solid red) and simulated curves (dashed dashed blue), which are based on the optimum 1 parameters.

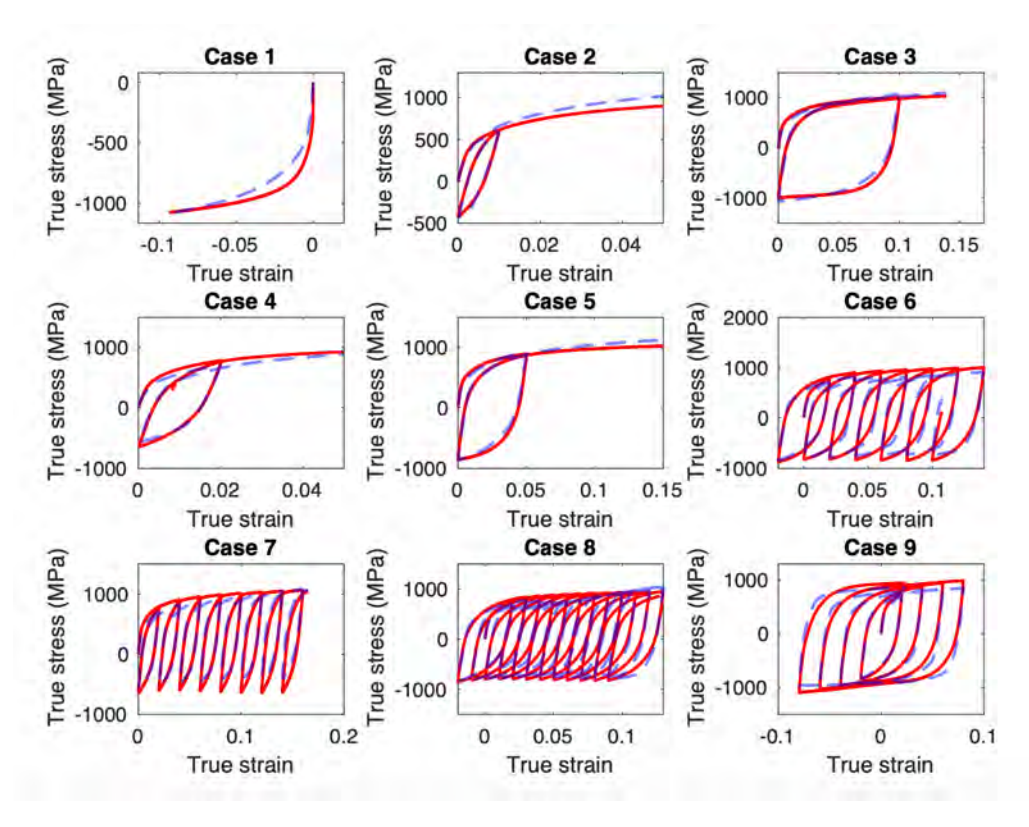


Figure 5: Comparison between experimental curves taken from [49] (solid red) and simulated curves (dashed blue), which are based on the optimum 2 parameters.

# 3.2 Application to SS316L

The EPSC model was also calibrated using the sequential infilling pipeline with experimental SS316L strain rate and temperature sensitive flow stress and phase fraction data. The ranking plot of the solutions is shown in appendix C. With a budget of 150, 14 parameters (additional 4 were fixed), and 7 straining conditions, the total number of simulation calls was 2,700—a little over 2 days on a single node with 4 cores. Parameters of  $\varepsilon$ -martensite are taken from the prior work [75] and set as constants because of its negligible volume fraction. The optimized set of parameters are shown in Table 5, and the objectives are shown in Figures 6–8. Figures 6 shows that the model is successfully calibrated to capture the effects of strain rate, while Figure 7 shows that the model is successfully calibrated to capture the effects of temperature on deformation behavior of the steel.

Figure 8 shows that the adjusted model correctly captures the expected trends in the evolution of phases, where the increase in temperature suppresses the rate of transformations. Since the transformed martensite volume fraction is essential for the deformation behavior of SS316L, we included the three data points as objectives (the one red data point is one objective, while the two green points are another objective) as shown in Table 1. However, it constitutes only a minor fraction in the overall error evaluation. Additionally, the difference between the measured data and the predictions is also attributed to the model formulation. We remind that the EPSC model formulation is a mean field type, which makes the model computationally efficient but reduces its predictive characteristics. Model modifications such as accounting for spreads in the field variables over ellipsoids can improve the predictions. In the current model formulation, a single value is assumed for a given field across the entire ellipsoid. The calculations of spreads have been incorporated into a visco-plastic SC (VPSC) formulation [76, 77, 78, 79, 80]. These model improvements are left for future works.

Table 5: EPSC model parameters for austenite and two martensite phases of SS316L steel identified using the developed Pareto-based multi-objective machine learning procedure for efficient identification of crystal plasticity model parameters. The initial slip resistances,  $\tau_0$ , of two martensite phases are assumed to be constant so only  $\tau_{0,a}$  term is used. The asterisk (\*) indicates parameters that were not optimized but set as constants based on prior fitting efforts [75] to better constrain the model. Crystal elastic constants for  $\gamma$ -austenite,  $\varepsilon$ -martensite, and  $\alpha'$ -martensite follow the values reported in [81, 82]:  $C_{11}^{\gamma}=209$  GPa,  $C_{12}^{\gamma}=133$  GPa,  $C_{44}^{\gamma}=121$  GPa,  $C_{11}^{\varepsilon}=269$  GPa,  $C_{12}^{\varepsilon}=129$  GPa,  $C_{44}^{\varepsilon}=49$  GPa, and  $C_{11}^{\alpha'}=234$  GPa,  $C_{12}^{\alpha'}=135$  GPa, and  $C_{44}^{\alpha'}=118$  GPa.

Parameters	$\gamma$ -Austenite	$\varepsilon ext{-Martensite}$	$\alpha'$ -Martensite	
$\kappa_1^{\alpha}[m^{-1}]$	1.19e+08	0.205e + 08*	1.12e + 08	
$g^{lpha}$	0.192	1.0e + 06*	0.211	
$D^{\alpha}[MPa]$	132.1	100*	356.3	
$\tau_{0,a}[MPa]$	351.6	800.0*	449.1	
$ au_{0,b}$	0.032	-	_	
$ au_{0,c}[K]$	257.3	-	_	
Phase transformation parameters				
[ m ] ]	0.4.400	C [m]]	10.050	

Thase transformation parameters				
$m_{SFE}[rac{mJ}{Km^{-2}}]$	0.1428	$C_{SFE}[\frac{mJ}{m^{-2}}]$	12.3507	
$\kappa_{eta}$	0.1883	$eta_0$	0.0603	

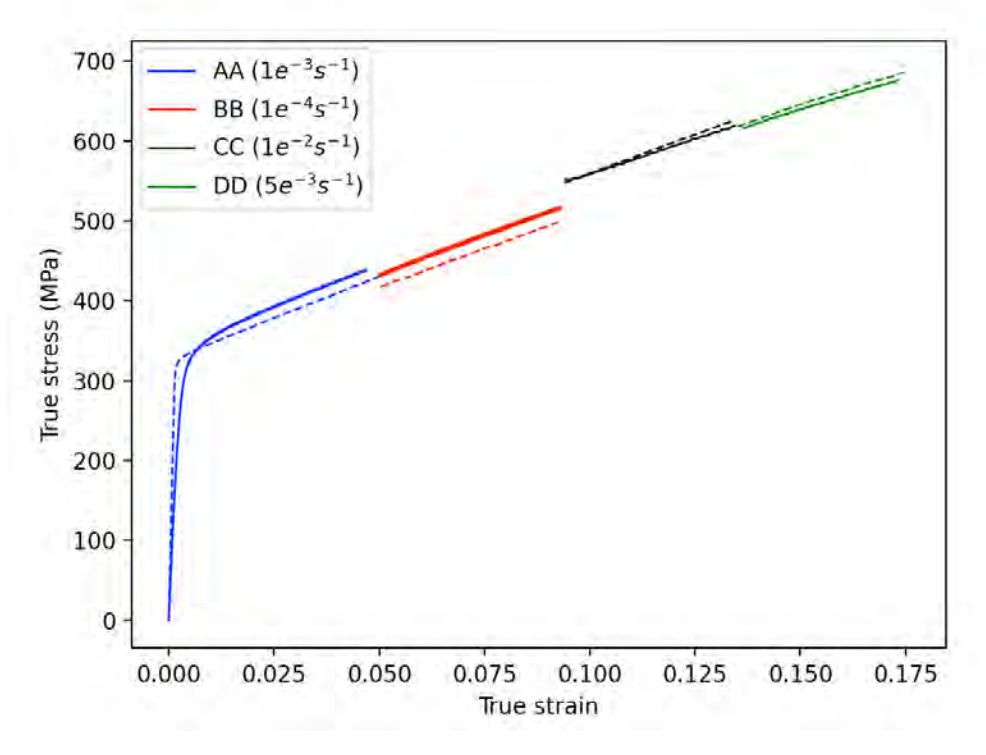


Figure 6: Comparison between experimental curves taken from [53] (solid lines) and simulated (dashed lines) curves with four jumps in strain rate at  $20~^{\circ}\text{C}$ .

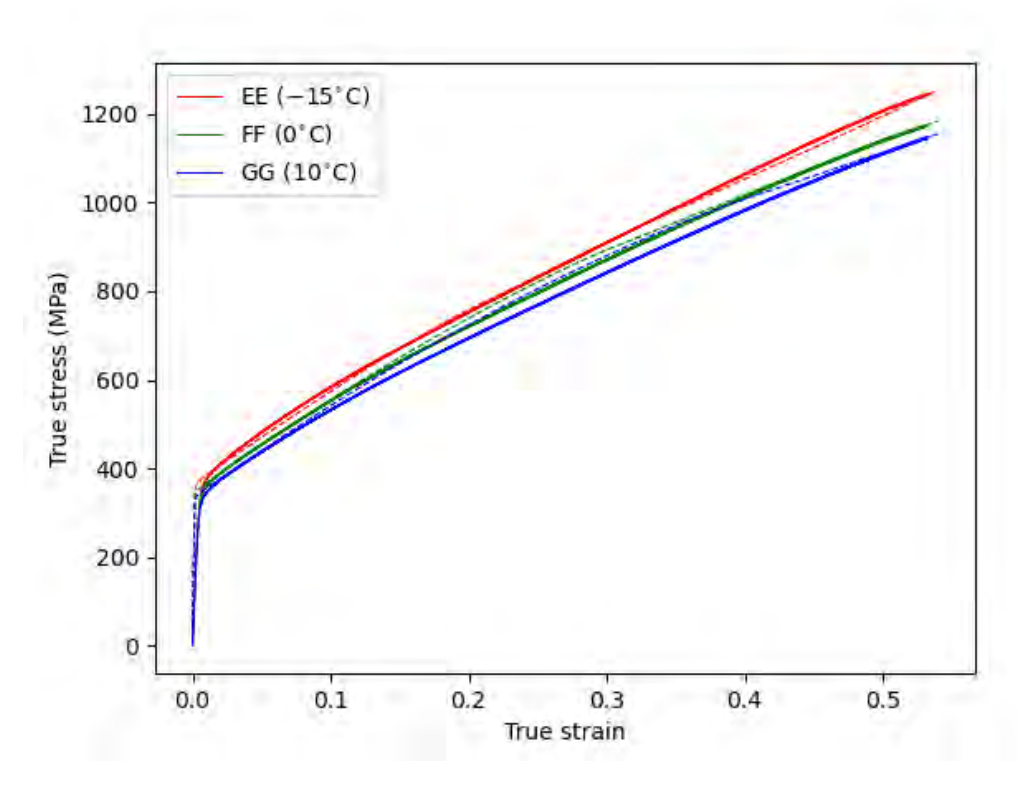


Figure 7: Comparison between experimental curves taken from [53] (solid lines) and simulated (dashed lines) curves at four temperatures under a strain rate of  $0.001\ s^{-1}$ .

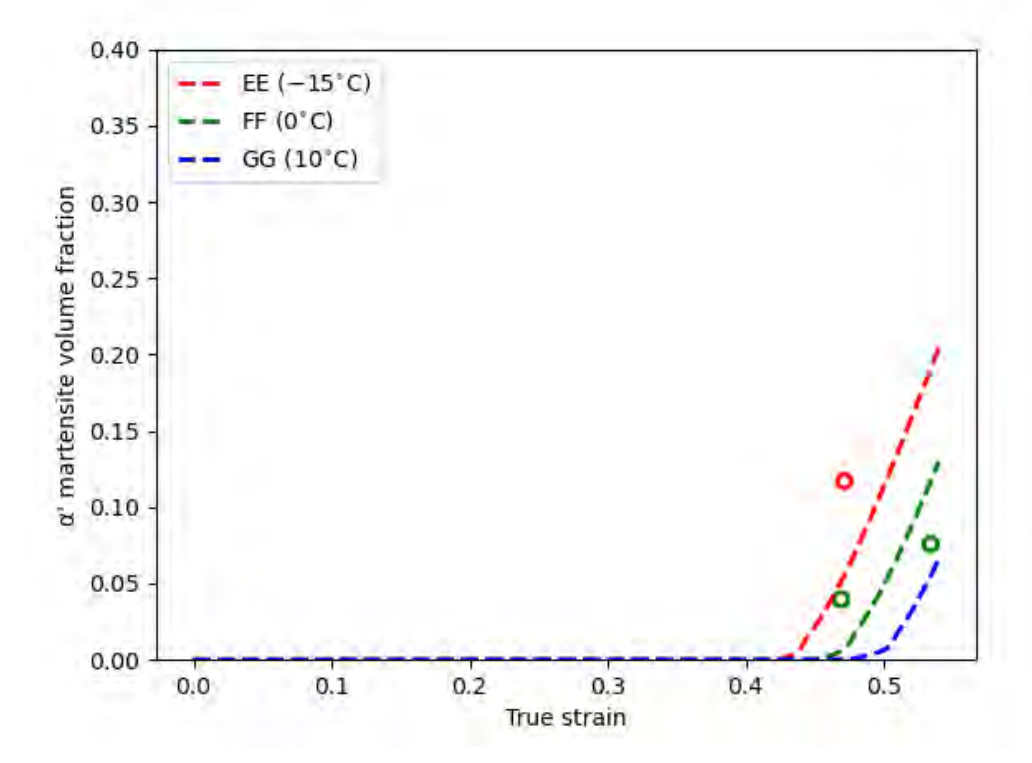


Figure 8: Comparison between experimental (discrete points) and simulated (dashed lines) fraction of  $\alpha'$ -martensite at four temperatures under a constant strain rate. The fraction of  $\varepsilon$ -martensite is nearly zero.

#### 3.3 Verification using biaxial tension of SS316L

The calibrated parameters of the EPSC model incorporating the dislocation density-based hardening law and the phase transformations law for modeling of the SS316L 1.2 mm sheets were used to simulate three biaxial tension cases of cruciform specimens for further verification. The details of the experimental procedures can be found in [55]. The FE model was an eighth of the specimen used in the experiments after invoking the symmetries in X-Y, X-Z, and Y-Z planes, as shown in Figure 9. The use of these symmetries is justified because of the typical orthotropic symmetry exhibited by rolled sheets. The selected mesh is a result of geometry partitioning and a mesh convergence study that reduced the mesh to 5064 C3D8R elements with 4 elements through-thickness. A displacement of 3.5 mm is applied to each arm in the rolling direction (RD) and transverse direction (TD), respectively, for the first simulation case of 4:4 strain path. Displacements of 1.75 mm and 3.5 mm are applied to the RD and TD arms, respectively, for the second simulation case of 2:4 strain path. Finally, a displacement of 3.5 mm is applied to the TD arm, while RD is fixed for the third simulation case of 0:4 strain path.

The underlying model used to simulate the three tests is the EPSC homogenization at the meso-level providing a constitutive response at each FE integration point, within the boundary value problem solved using the implicit FEM at the macro-level in Abaqus [83]. A brief summary of the coupled modeling framework is given in appendix A. The FE-EPSC microstructure sensitive simulations predicted mechanical fields along with the transformed volume fractions of  $\alpha$ '-martensite and texture evolution. The material at each integration point in the finite element model is represented with the same 500 grains as in the earlier standalone simulations using EPSC. The rate of transformations is driven by mechanical fields, i.e., the local states of stress, strain, and stress-triaxiality (the ratio between mean stress and von Mises stress), as described in the appendix. Figures 10–12 present the predicted triaxiality, effective strain, von Mises stress, and volume fraction of  $\alpha'$ -martensite distributions as contours over the meshed model for each of the strain path cases. The model is mirrored in the X-Z and Y-Z planes for visualization. Although the higher triaxiality regions of the model should promote the transformed volumes, those regions have stress and strain states underdeveloped in comparison with the regions near the notches. Since stress/strain states in grains directly govern the rate of transformations, as described in the appendix, the high stress regions develop the highest  $\alpha$ '-martensite fractions. Figure 13 shows microstructure in the steel before and after equi-biaxial deformation at the location indicated in 10. The data was acquired using electron back-scattered diffraction (EBSD). The phase map verifies the predicted fraction of  $\alpha$ '-martensite after deformation.

Finally, Figure 14a-c compare the experimental and simulated force versus displacement for each case, while Figure 14d compares the strain path at the center of the pocket per specimen. The strain path is plotted as the strain in TD versus the strain in RD. Evidently, these results also show good agreement between the simulations and the experiments, verifying the model and identified parameters.

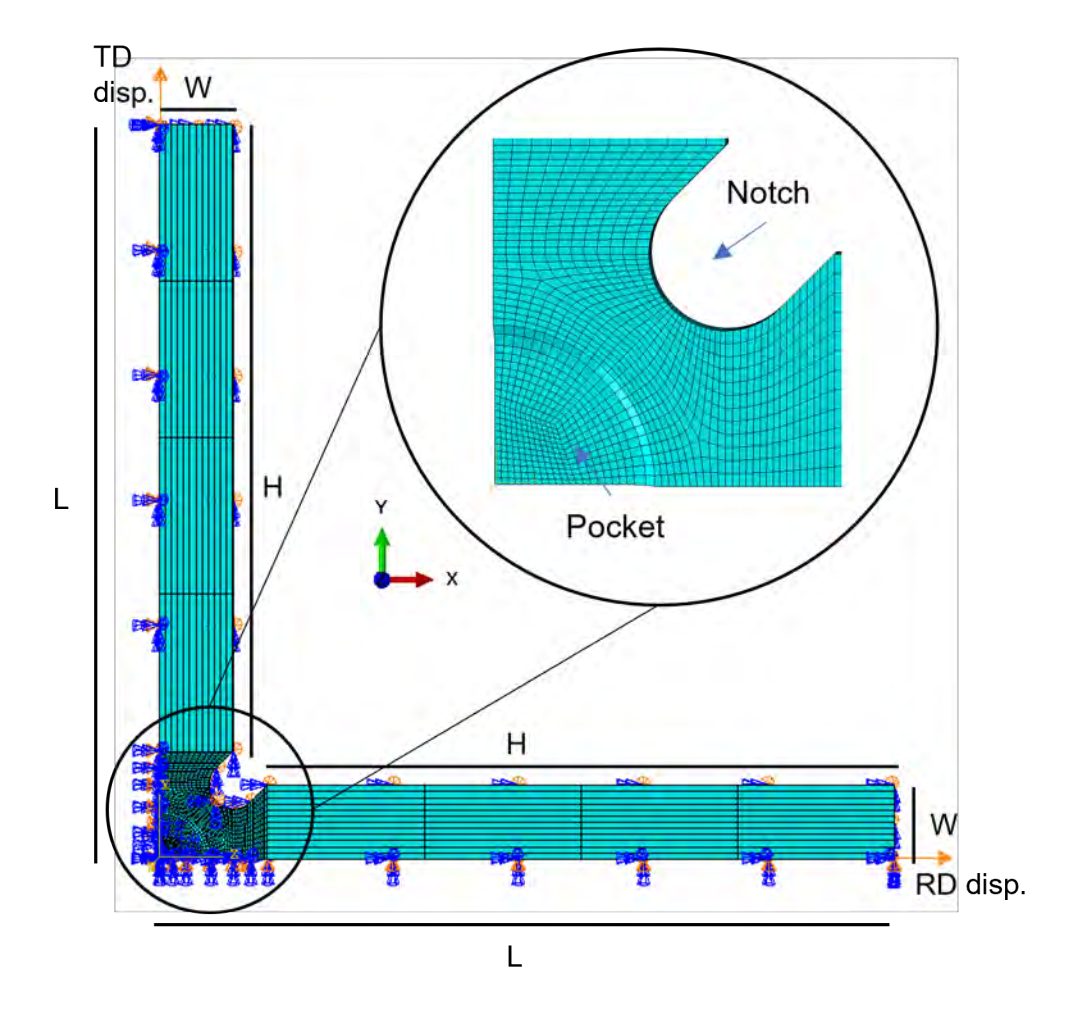


Figure 9: One-eighth of the cruciform specimen displaying important dimensions to appreciate the scale ( $L=75~\mathrm{mm},~H=64~\mathrm{mm},~\mathrm{and}~W=7.5~\mathrm{mm}$ ) and boundary conditions for meshing in Abaqus. Displacement boundary conditions are applied on each arm and symmetry boundary conditions are applied on the inner surfaces.

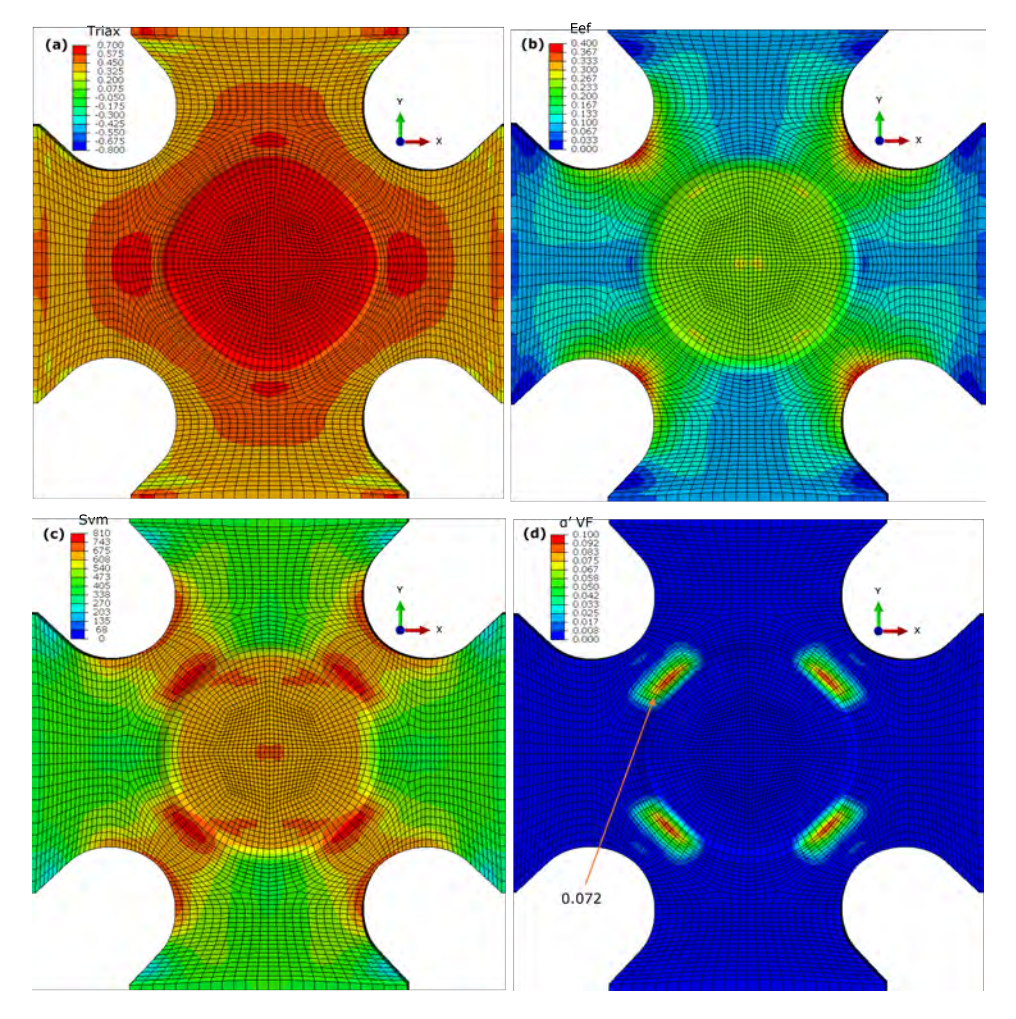


Figure 10: Contours of (a) stress triaxiality, (b) effective strain, (c) von Mises stress, and (d) volume fraction of evolved  $\alpha$ '-martensite over the mesh for the equi-biaxial (4:4) strain path case. The arrow shows the location where the EBSD scan was taken. The model predicts 0.072 fraction of  $\alpha$ '-martensite at that location.

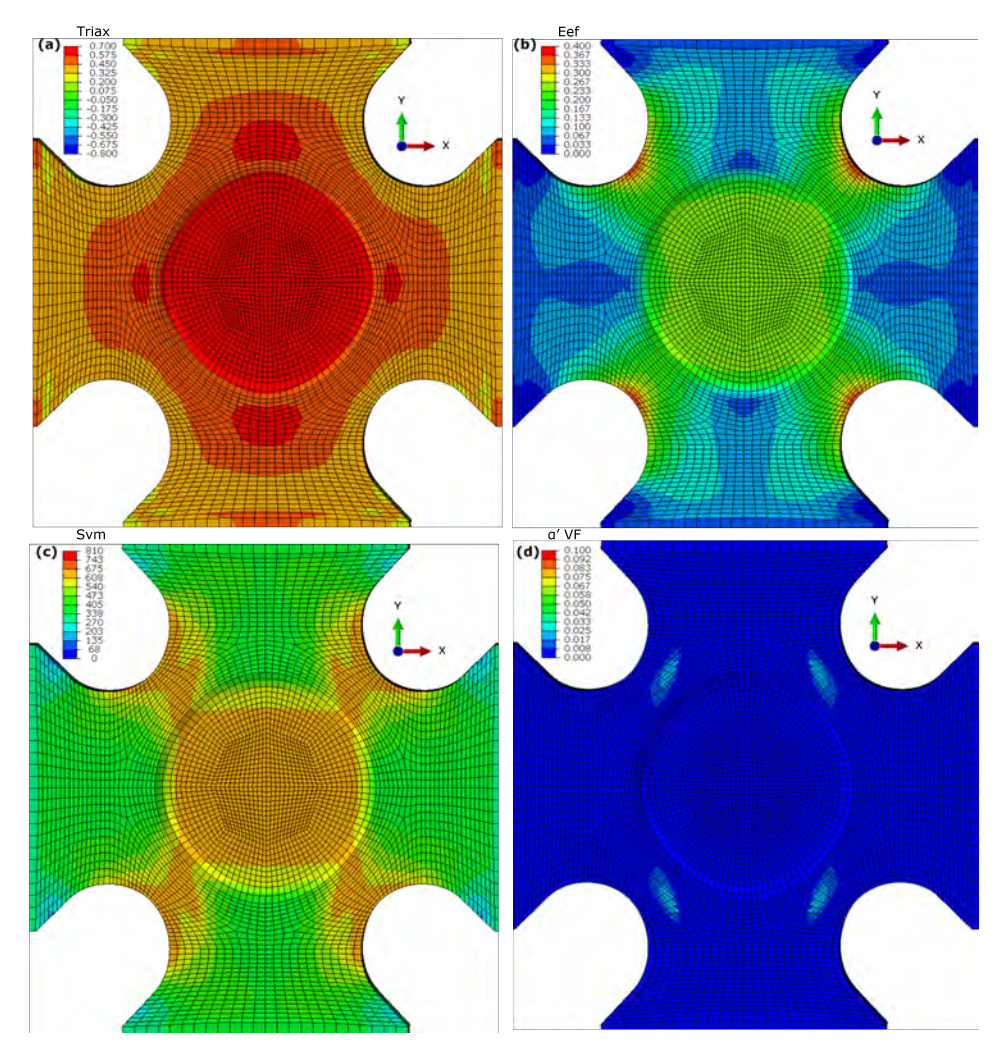


Figure 11: Contours of (a) stress triaxiality, (b) effective strain, (c) von Mises stress, and (d) volume fraction of evolved  $\alpha$ '-martensite over the mesh for the 2:4 strain path case.

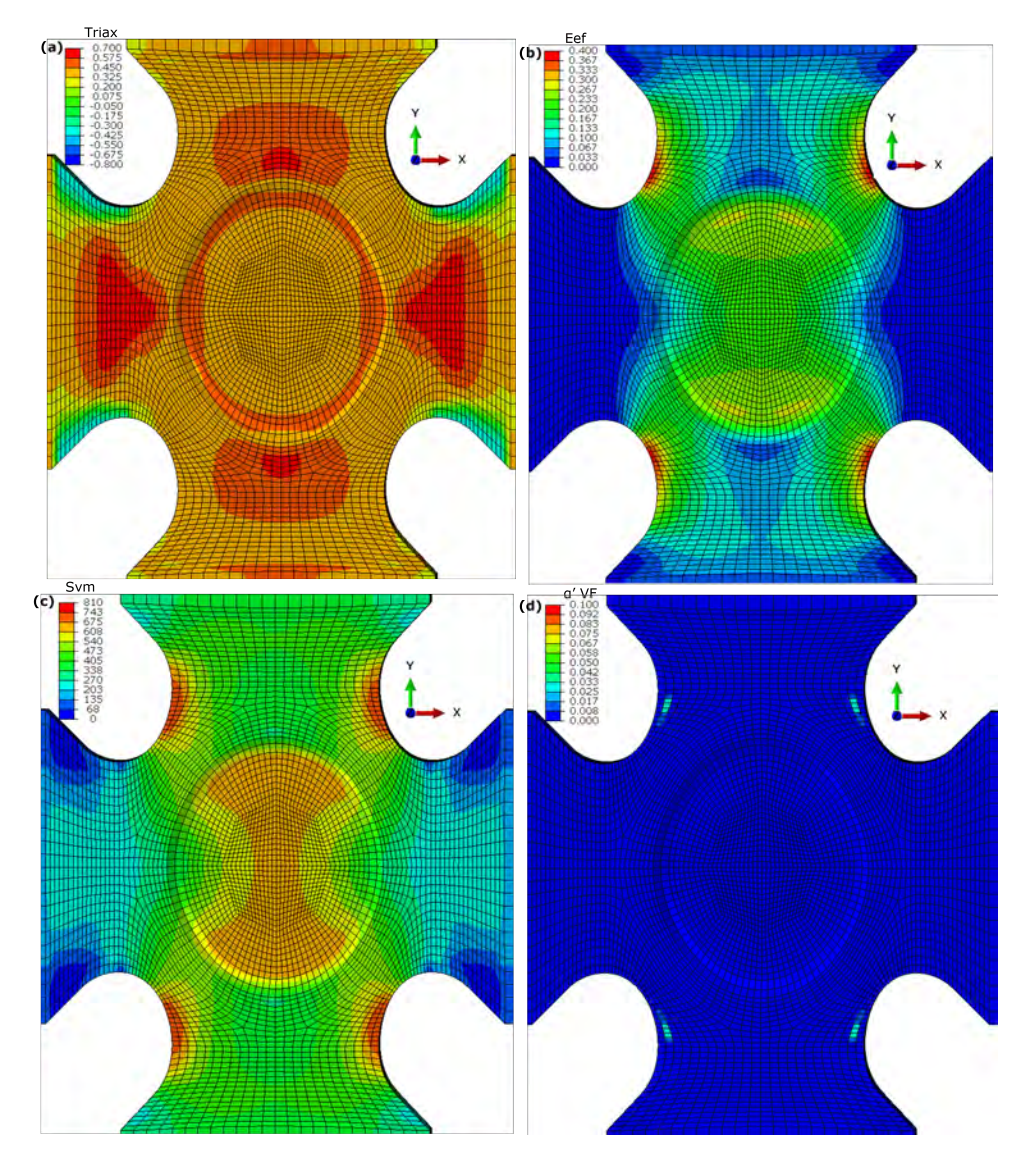


Figure 12: Contours of (a) stress triaxiality, (b) effective strain, (c) von Mises stress, and (d) volume fraction of evolved  $\alpha$ '-martensite over the mesh for the 0:4 strain path case.

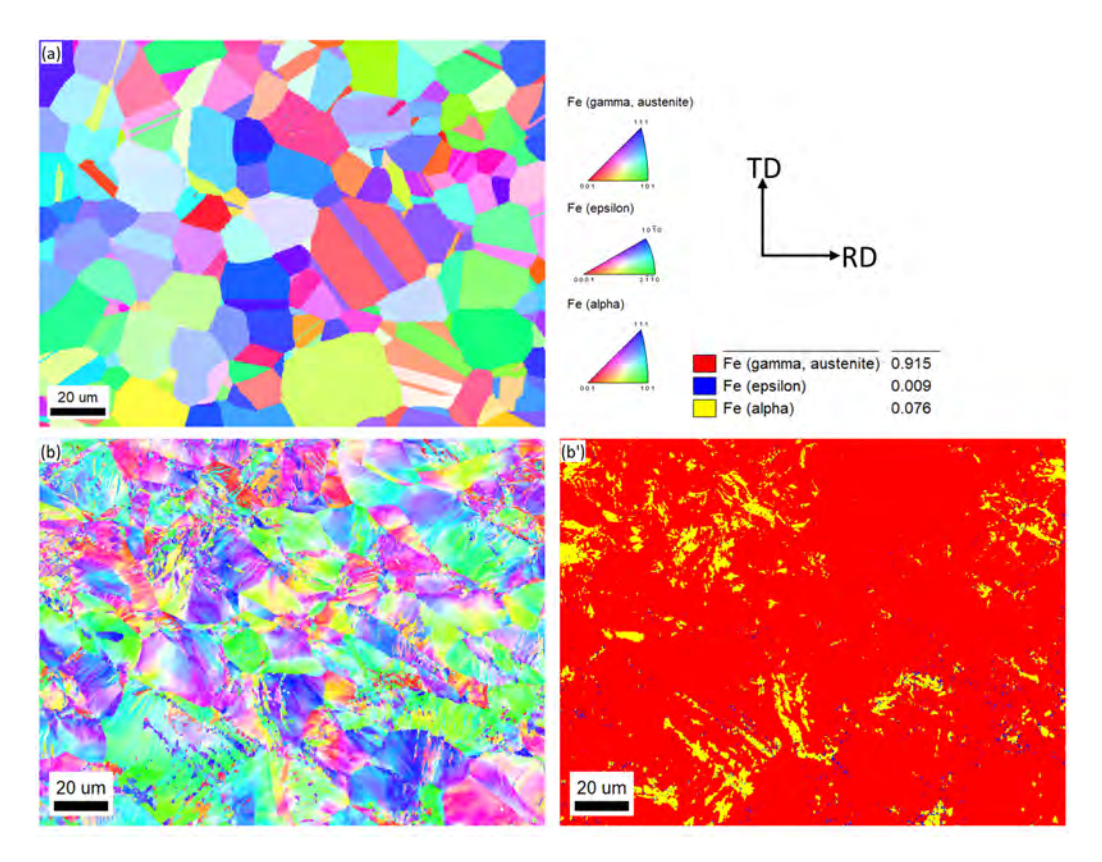


Figure 13: Inverse pole figure (IPF) maps measured here to show grain structure in the steel, SS316L: (a) initial and (b) after equi-biaxial tension to approximately 0.35 displacement at the location indicated in Figure 10. (b') phase map showing the fraction of phases in the structure shown in (b).

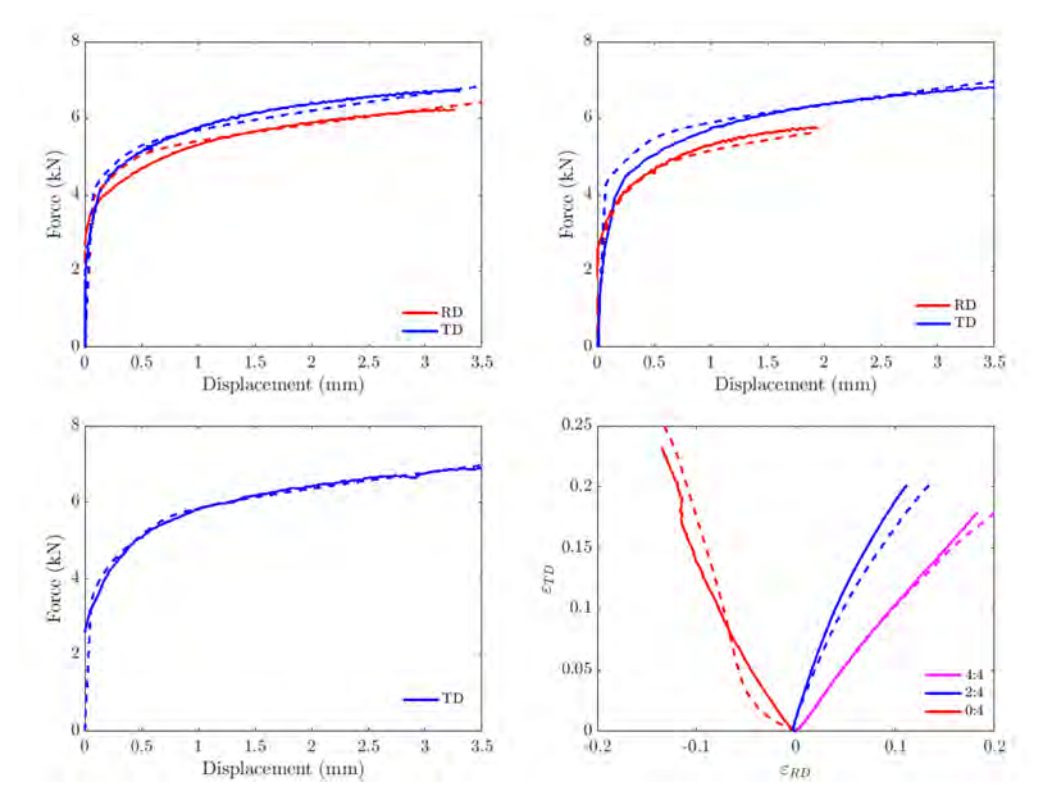


Figure 14: Experimental from [55] (solid lines) and simulated (dashed lines) force vs displacement curves recorded during biaxial tension along RD and TD directions for the three strain path cases: (a) 4:4, (b) 2:4, and (c) 0:4. (d) Corresponding strain paths at the center of the cruciform specimen for the three cases.

# 4 Conclusions

In this work, the first machine learning-based multi-objective optimization procedure is developed for efficient identification of crystal plasticity model parameters. Specifically, a GP-based budgeted multi-objective optimization sequential infilling algorithm is implemented in a Python and R application to identify the constitutive parameters of the EPSC crystal plasticity model featuring a dislocation density-based hardening, a slip system-level kinematic back-stress, and a phase transformation sub-models. The utility of the developed application was demonstrated by identifying model parameters for two steel alloys, DP780 and SS316L. Experimental flow stress data for nine complex strain paths were used as objectives to identify the parameters for DP780 steel. Experimental flow stress and phase fractions data for eight tensile tests in function of strain-rate and temperature were used as objectives to identify parameters for SS316L. A budget value of 150 was found to be sufficient to determine Pareto-optimal points (constitutive parameters) for both alloys. Significantly, the number of runs of the expensive black-box function (objectives based on the crystal plasticity model) reduced by approximately two orders of magnitude using the novel machine learning-based procedure in comparison to the former GA-based procedure. The parameters identified for SS316L were critically verified by simulating three biaxial tensile loading paths using FE-EPSC.

# 5 Data availability

The raw data and archived git repository associated with this work can be found at https://github.com/galois17/py\_infill\_pipeline\_v2 or https://github.com/galois17/py\_infill\_pipeline.

# 6 Acknowledgments

This research was sponsored by the U.S. National Science Foundation and accomplished under the OIA-1757371 grant.

# Appendix A: Summary of the EPSC model

This appendix summarizes the main equations pertaining to the implicit EPSC model formulation along with the dislocation-based hardening [84, 85], slip systemlevel kinematic back-stress [86], and phase transformations [75] sub-models. Coupling of the model with Abaqus through the use of a user material subroutine (UMAT) named as FE-EPSC is also briefly described [67]. The emphasis of the description is on the role of parameters in the constitutive response, as these parameters are used in the optimization procedures. In this section, dot and tensor products are indicated by  $\bullet$  and  $\otimes$ , respectively.

# Constitutive equations

The EPSC constitutive formulation relates the Jaumann rate of Cauchy stress,  $\hat{\sigma}$ , with strain rate,  $\dot{\boldsymbol{\epsilon}}$ :

$$\hat{\sigma} = \dot{\sigma} + \sigma \mathbf{W} - \mathbf{W} \sigma, \tag{A.1}$$

where  $\sigma$  and W are the Cauchy stress and spin tensors. The constitutive equation is applied at a material point, which can be a single crystal or a polycrystal i.e. a representative volume element (RVE). At the crystal level, the respective quantities are denoted as  $\sigma^c$  and  $\mathbf{W}^c$  for a single crystal, c. The Jaumann rate of Cauchy stress,  $\hat{\sigma}^c$ , and strain rate,  $\dot{\epsilon}^c$ , are related by the following constitutive relation:

$$\hat{\boldsymbol{\sigma}}^c = \mathbf{C}^c(\dot{\boldsymbol{\epsilon}}^c - \dot{\boldsymbol{\epsilon}}^{pl,c} - \dot{\boldsymbol{\epsilon}}^{pt,c}) - \boldsymbol{\sigma}^c \operatorname{tr}(\dot{\boldsymbol{\epsilon}}^c), \tag{A.2}$$

where  $\mathbf{C}^c$  is the 4th rank single crystal elastic stiffness tensor,  $\dot{\boldsymbol{\epsilon}}^{pl,c}$  is the plastic strain-rate, and  $\dot{\boldsymbol{\epsilon}}^c$  is the total strain-rate. The phase transformation mechanics contribution is the phase transformation strain rate,  $\dot{\boldsymbol{\epsilon}}^{pt,c}$  [9]. The plastic strain rate is the sum of the products of Schmid tensors,  $\mathbf{m}^s = (1/2)(\mathbf{b}^s \otimes \mathbf{n}^s + \mathbf{n}^s \otimes \mathbf{b}^s)$ , and shearing rates,  $\dot{\gamma}^s$ , of all slip systems, s, in each single crystal. In EPSC, the crystal constitutive relation is written alternatively as:

$$\hat{\boldsymbol{\sigma}}^c = \mathbf{L}^c(\dot{\boldsymbol{\epsilon}}^c - \dot{\boldsymbol{\epsilon}}^{pt,c}),\tag{A.3}$$

where  $\mathbf{L}^c$  is the crystal elasto-plastic stiffness tensor derived from Eq. (A.2) and a selected hardening law for the evolution of slip resistance [87, 88]. The selfconsistent homogenization procedure then gives rise to the constitutive relation at the polycrystal level starting from the volume average quantities for stress and strain over constituent crystals [1, 65].

# Dislocation density-based hardening law

The activation of slip systems follows the consistency criteria:

$$\boldsymbol{\sigma}^{c} \cdot \mathbf{m}^{s} = \tau_{c}^{s} \tag{A.4}$$

$$\hat{\boldsymbol{\sigma}}^{c} \cdot \mathbf{m}^{s} = \dot{\tau}_{c}^{s}, \tag{A.5}$$

$$\hat{\boldsymbol{\sigma}}^{\boldsymbol{c}} \cdot \mathbf{m}^{s} = \dot{\tau}_{c}^{s},\tag{A.5}$$

to ensure the stress is on the yield surface and remains on the yield surface for every constituent crystal [89]. Here  $\tau_c^s$  is the critical resolved shear stress per slip system in each single crystal and evolves with shear strain:

$$\dot{\tau}_c^s = \sum_{s'} h^{ss'} \dot{\gamma}^{s'},\tag{A.6}$$

where  $h^{ss'}$  is the hardening matrix describing the hardening effect of each slip system, s, on other slip systems, s', and  $\dot{\gamma}^{s'}$  is the shear strain rate per slip system per crystal. The total slip resistance of each slip system is:

$$\tau_c^s = \tau_0^\alpha + \tau_{forest}^s + \tau_{debris}^\alpha, \tag{A.7}$$

where  $\tau_0^{\alpha}$  is a strain-rate and temperature dependent initial slip resistance for slip modes  $\alpha$ :

$$\tau_0^{\alpha}(\dot{\epsilon}, T) = \tau_{0,a}^{\alpha} (1 + \tau_{0,b}^{\alpha} \log(\dot{\epsilon})) \exp\left(-\frac{T}{\tau_{0,c}^{\alpha}}\right), \tag{A.8}$$

with fitting parameters:  $\tau_{0,a}^{\alpha}$ ,  $\tau_{0,b}^{\alpha}$  and  $\tau_{0,c}^{\alpha}$ . The last two scale the contributions from strain-rate and temperature, respectively.  $\tau_{forest}^{s}$  and  $\tau_{debris}^{\alpha}$  are strain hardening contributions from evolution of forest and debris dislocations, respectively. The forest term accounts for the effects of statistically stored dislocations,  $\rho_{tot}^{s}$ , per slip system:

$$\tau_{forest}^{s} = b^{\alpha} \chi \mu^{\alpha} \sqrt{\sum_{s'} \mathcal{L}^{ss'} \rho_{tot}^{s'}}, \tag{A.9}$$

where  $b^{\alpha}$  is the Burgers vector,  $\chi$  is the interaction constant set to 0.9 for all phases,  $\mu^{\alpha}$  is the shear modulus, and  $\mathcal{L}^{ss'}$  is the strength interaction matrix with values set to 1 [90, 91]. The debris term accounts for the effects of debris dislocation density,  $\rho_{deb}$ , per slip mode that evolves with increasing deformation in the material:

$$\tau_{debris}^{\alpha} = 0.086 \mu^{\alpha} b^{\alpha} \sqrt{\rho_{deb}} \log \left( \frac{1}{b^{\alpha} \sqrt{\rho_{deb}}} \right). \tag{A.10}$$

The dislocation densities evolve with shear strain for each slip system in each grain. Additionally, the total forest dislocation density per slip system,  $\rho_{tot}^s$ , starts to evolve from an initial value,  $\rho_0^s$ , which is optimized in the DP cases but set to  $3.0\mathrm{e}+11~m^{-2}$  for the SS case. The forest dislocation density evolves with shear strain, strain rate, and temperature:

$$\frac{\partial \rho_{tot}^s}{\partial \gamma^s} = \kappa_1^{\alpha} \sqrt{\sum_{s'} g^{ss'} \rho_{tot}^{s'}} - \kappa_2^{\alpha} (\dot{\epsilon}, T) \rho_{tot}^s. \tag{A.11}$$

Here,  $\kappa_1^{\alpha}$  is the rate of dislocation generation,  $g^{ss'}$  is the slip system interaction matrix taken as an identity matrix, and  $\kappa_2^{\alpha}$  is a strain rate and temperature dependent dynamic recovery term derived as [84]:

$$\frac{\kappa_2^{\alpha}}{\kappa_1^{\alpha}} = \frac{\chi_b^{\alpha}}{g^{\alpha}} \left( 1 - \frac{\kappa_B T}{D^{\alpha} b^{\alpha}} \ln \left( \frac{\dot{\epsilon}}{\dot{\epsilon}_0} \right) \right), \tag{A.12}$$

where  $g^{\alpha}$  is the normalized activation energy,  $\kappa_B$  is the Boltzmann constant,  $D^{\alpha}$  is the drag stress, and  $\dot{\epsilon}_0 = 10^7 s^{-1}$  is the reference strain-rate. Finally, the debris dislocation density evolves with shear strain, strain-rate, and temperature as:

$$\frac{\partial \rho_{deb}}{\partial \gamma^s} = q^{\alpha} b^{\alpha} \sqrt{\rho_{deb}} \kappa_2^{\alpha} (\dot{\epsilon}, T) \rho_{tot}^s, \tag{A.13}$$

where  $q^{\alpha} = 4$  is a constant for the dislocation recovery rate. The initial debris dislocation density is set to a small value of 0.1  $m^{-2}$ .

#### A.3 Backstress law

This section describes the backstress formulation used in the modeling of cyclic loading of DP780 steel. More details can be found in [86, 49]. The backstress is evolved on each slip system in ferrite grains as a function of shear strain during forward loading. Consider the case of shearing in the positive slip direction of a slip system,  $\gamma^{s+} > 0$ , with positive amount of accumulated backstress  $\tau^{s+}_{bs.sys} > 0$ :

$$\tau_{bs,sys}^{s+} = \tau_{bs}^{sat} (1 - \exp(-\nu \gamma^{s+})),$$
 (A.14)

$$\tau_{bs,sys}^{s-} = -A\tau_{bs,sys}^{s+},\tag{A.15}$$

(A.16)

On the other hand, in the case of  $\gamma^{s+} > 0$  and  $\tau^{s+}_{bs,sys} < 0$ , we have:

$$\tau_{bs,sys}^{s+} = -(A+1)\tau_{bs}^{sat} \exp(-\frac{\gamma^{s+}}{\gamma_b}) + \tau_{bs}^{sat}, \tag{A.17}$$

$$\tau_{bs,sys}^{s-} = -\frac{1}{A}\tau_{bs,sys}^{s+}. (A.18)$$

In the above equations,  $\tau_{bs,sys}^{s+}$  and  $\tau_{bs,sys}^{s-}$  are the backstresses accumulated in the positive and negative directions of a slip system, respectively,  $\tau_{bs}^{sat}$  is the saturated backstress,  $\gamma_b$  and  $\nu$  are fitting coefficients, and A is a parameter for asymmetric evolution of backstress in the two opposite directions,  $s^+$  and  $s^-$ . Backstress acts in the opposite direction of the current direction of slip and reduces the critical resolved shear stress needed to activate the slip when the direction flips upon load reversal. The modified Eq. (A.4a) describes this effect:

$$\boldsymbol{\sigma}^c \cdot \mathbf{m}^{s-} - \tau_{bs}^{s+} = \tau_c^{s-}. \tag{A.19}$$

Given that the overall backstress must vanish in the RVE, the backstress in martensite regions is defined using the volume average of backstress in the ferrite phase [86, 49].

## A.4 Phase transformations law

The strain-induced FCC  $\gamma$ -austenite to BCC  $\alpha'$ -martensite phase transformation begins with the formation of shear bands [92] as partial dislocations on austenite slip systems separate to form a sufficiently thick stacking fault. The key equations are summarized in this section while more details can be found in [9, 75].

The stacking fault width is:

$$d = cN^2/(2\gamma_N - Nb_n((\hat{\mathbf{b}}_l^s - \hat{\mathbf{b}}_r^s)\boldsymbol{\sigma}^c) \cdot \hat{\mathbf{n}}^s), \tag{A.20}$$

where c is a constant, N is the number of faults in the shear band,  $\gamma_N$  is the fault energy,  $b_p = \frac{\alpha_{\gamma}}{\sqrt{6}}$  is the magnitude of the Burgers vector of a partial dislocation,  $\hat{\mathbf{b}}_l^s$  and  $\hat{\mathbf{b}}_r^s$  are the unit vectors of the left and right partial dislocations, respectively, and  $\hat{\mathbf{n}}^s$  is the normal vector of the slip plane. To reach a large partial separation, the denominator approaches zero:

$$\frac{2\gamma_N}{N} - b_p((\hat{\mathbf{b}}_l^s - \hat{\mathbf{b}}_r^s)\boldsymbol{\sigma}^c) \cdot \hat{\mathbf{n}}^s = 0$$
(A.21)

where  $\frac{\gamma_N}{N}$  is the stacking fault energy (SFE), which is a material constant and can be experimentally measured. The shear band has an HCP structure, which is

known as the  $\varepsilon$ -martensite. As each slip system can form a shear band through partial separation and multiple slip systems can be active in each austenite grain, multiple shear bands in a grain intersect and form  $\alpha'$ -martensite at the intersection. Since the transformation is derived from slip activity in the FCC grain, the volume increase of 2.59% [81] between FCC and BCC structure gives rise to the phase transformation strain,  $\epsilon^{pt}$ , through the volumetric part of the Bain deformation gradient,  $\mathbf{F}^{vol}$  [93, 94]:

$$\epsilon^{pt} = \frac{(\mathbf{F}^{vol})^T \mathbf{F}^{vol} - \mathbf{I}}{2}.$$
(A.22)

The deformation mechanics phase transformation model in EPSC nucleates the shear bands as  $\varepsilon$ -martensite grains. The volume fraction increment,  $\Delta f^{s,\varepsilon}$ , is:

$$\Delta f^{s,\varepsilon} = \frac{\Delta \gamma^{s,p}}{s^{\epsilon}} \tag{A.23}$$

where  $\Delta \gamma^{s,p}$  is the shear strain increment and  $s^{\varepsilon}$  is the characteristic shear relating  $\gamma$ -austenite to  $\epsilon$ -martensite derived from the intrinsic twinning shear,  $s^{tw}$  [95]:

$$s^{\varepsilon} = \frac{s^{tw}}{2} = \frac{1}{2\sqrt{2}}.\tag{A.24}$$

The effect of triaxiality on transformation rate is introduced via  $\beta = \beta_0 + x_\beta(\sigma^c)\kappa_\beta$ , which follows the formulations in an earlier Olson-Cohen phase transformation EPSC model [9], and scales the  $\varepsilon$ -martensite volume fraction increment.

As observed in the SS316L temperature-dependence data, the onset of transformation is delayed at higher temperatures, suggesting material under higher temperatures have higher SFE parameters, which is also consistent with earlier reports [96, 97] that also reported the SFE to vary linearly with temperature. Therefore, the effect of temperature on transformation is introduced via  $\frac{\gamma_N}{N} = m_{SFE}(T-273.15) + C_{SFE}$ , where the intercept  $C_{SFE}$  is the SFE at a reference temperature T=273.15K and the slope  $m_{SFE}$  is the temperature sensitivity coefficient.

Then, the  $\alpha'$ -martensite volume fraction increment incorporating shear strain increment on the HCP transformation plane,  $\Delta \gamma^s$ , and characteristic shear for the  $\varepsilon \to \alpha'$  transformation,  $s^{\varepsilon \to \alpha'} = \frac{1}{3\sqrt{2}}$ , is:

$$\Delta f^{s,\alpha'} = \frac{\Delta \gamma^s}{s^{\varepsilon \to \alpha'}} \tag{A.25}$$

Both  $\varepsilon$ -martensite and  $\alpha'$ -martensite grains are nucleated when the volume reaches 0.01. Multiple FCC slip systems can nucleate independent HCP  $\varepsilon$ -martensite grains per parent austenite grain. However, only the geometries of the two largest HCP shear bands give rise to the orientation of the resulting  $\alpha'$ -martensite grain. Subsequently transformed  $\alpha'$ -martensite from all sources in the same parent austenite grain are assumed to re-orient to match the first  $\alpha'$  grain and the volume fractions contribute to the volume fraction of the first  $\alpha'$ -martensite grain. Upon nucleation, the new grains inherit the current crystal states from the parent austenite grain such as dislocation density, stress, and strain. The crystallographic orientation relationship between austenite,  $\varepsilon$ -martensite, and  $\alpha'$ -martensite is:  $\{111\}_{\gamma} \parallel \{0001\}_{\varepsilon} \parallel \{110\}_{\alpha'}$  with  $\langle 110\rangle_{\gamma} \parallel \langle 2\bar{1}\bar{1}0\rangle_{\varepsilon} \parallel \langle 111\rangle_{\alpha'}$ .

#### A.5 FE-EPSC

The FE-EPSC model interacts with the FE analysis software, Abaqus, through the UMAT subroutine. The subroutine passes an imposed strain increment and a state variables array at each FE integration point, while the FE-EPSC model returns the homogenized stress tensor, Jacobian matrix, and updated state variables. Every integration point in the finite element mesh is initially given the same model parameters and texture. The texture and phase fractions evolve with plastic strain. In each simulation time, t, Abaqus sends a strain increment,  $\Delta \epsilon_{FE}^t$ , determined from the boundary conditions imposed onto the mesh, and the FE-EPSC follows the constitutive law to calculate the corresponding homogenized stress,  $\sigma_{FE}^{t+\Delta t}$ . The accumulated strain at the current time, t, is:

$$\epsilon_{FE}^{t+\Delta t} = \epsilon_{FE}^t + \Delta \epsilon_{FE}. \tag{A.26}$$

The Jacobian matrix,  $\frac{\partial \Delta \sigma_{FE}}{\partial \Delta \epsilon_{FE}}$ , derived in [83] is also returned to Abaqus to estimate subsequent trial displacement fields. It is the stiffness,  $\bar{\mathbf{L}}^{inc}$ , that relates Cauchy stress and strain:

$$\frac{\partial \Delta \sigma_{FE}}{\partial \Delta \epsilon_{FE}} = \frac{\partial (\sigma_{FE}^{t+\Delta t} - \sigma_{FE}^{t})}{\partial \Delta \epsilon_{FE}} = \frac{\partial \Delta \bar{\sigma}}{\partial \Delta \bar{\epsilon}} = \frac{\partial (\bar{\mathbf{L}}^{inc} \Delta \bar{\epsilon})}{\partial \Delta \bar{\epsilon}} = \bar{\mathbf{L}}^{inc}$$
(A.27)

# B Appendix B: Initial texture

This appendix presents pole figures showing the initial texture in the studied alloys (Figure 15 and Figure 16).

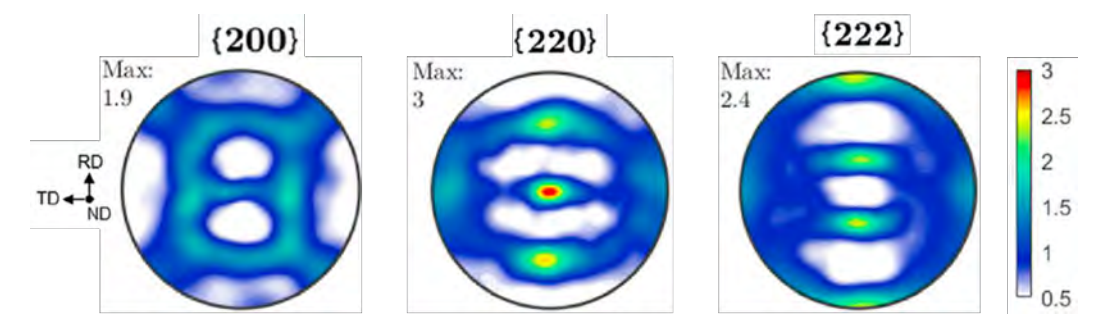


Figure 15: Pole figures showing the initial texture of DP780.

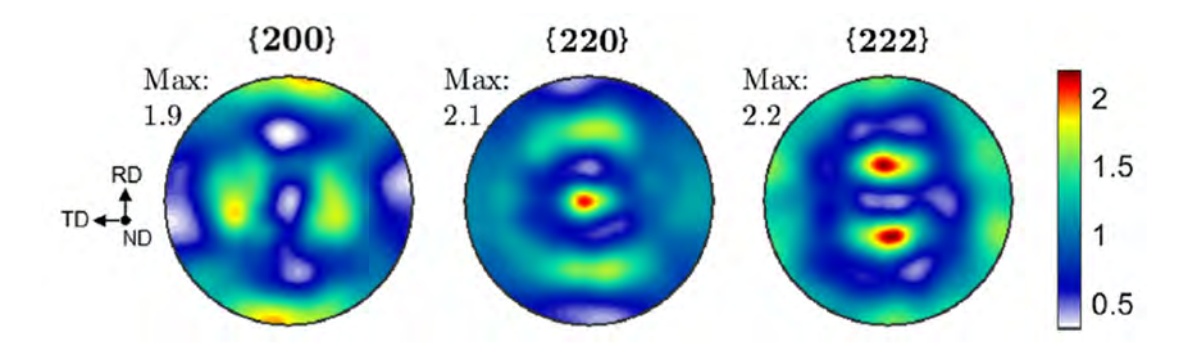


Figure 16: Pole figures showing the initial texture of SS316L.

# C Appendix C: RMSE

This appendix presents normalised RMSE to get percent error followed by averaging over objectives per material, which is used to rank the identified Pareto optima

(Figure 17a and Figure 17b). An example not normalised RMSE for each out of 9 objectives for the DP780 case study is: 36.5823 41.7893 41.6133 21.8229 24.4985 32.6111 39.3297 40.8595 46.6604 in (MPa). Note that every experimental curve and corresponding simulated curve are discretized into many points to ger RMSE per objective. Figure 18, Figure 19, and Figure 20 show the simulation results corresponding to the lowest point on the plot in Figure 17b (optimum 2). Table 6 are parameters for optimum 2.

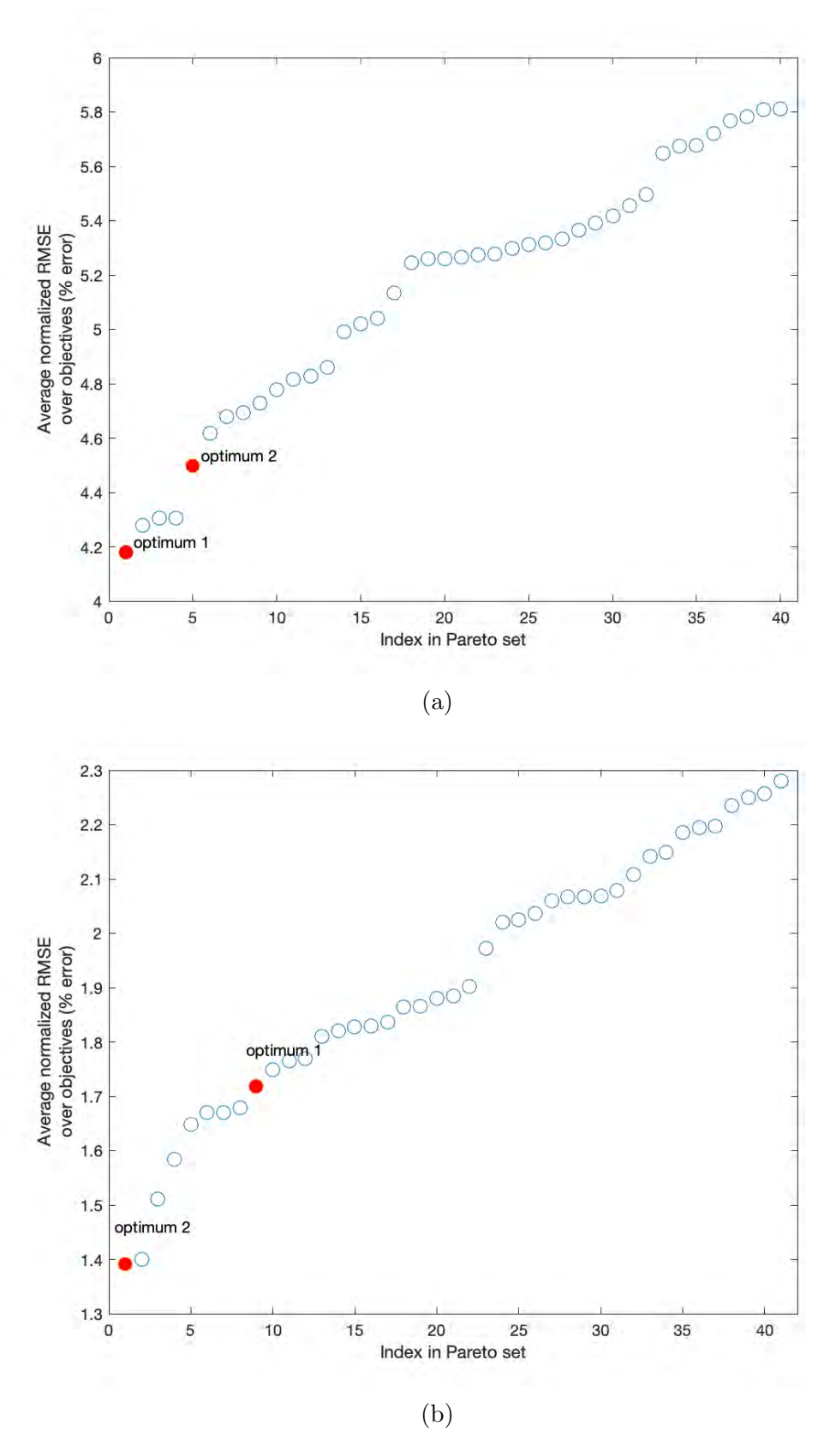


Figure 17: Average normalized RMSE sorted in an ascending order for: (a) Pareto set containing 40 optimal solutions for parameters of DP780 and (b) Pareto set containing 41 optimal solutions for parameters of SS316L.

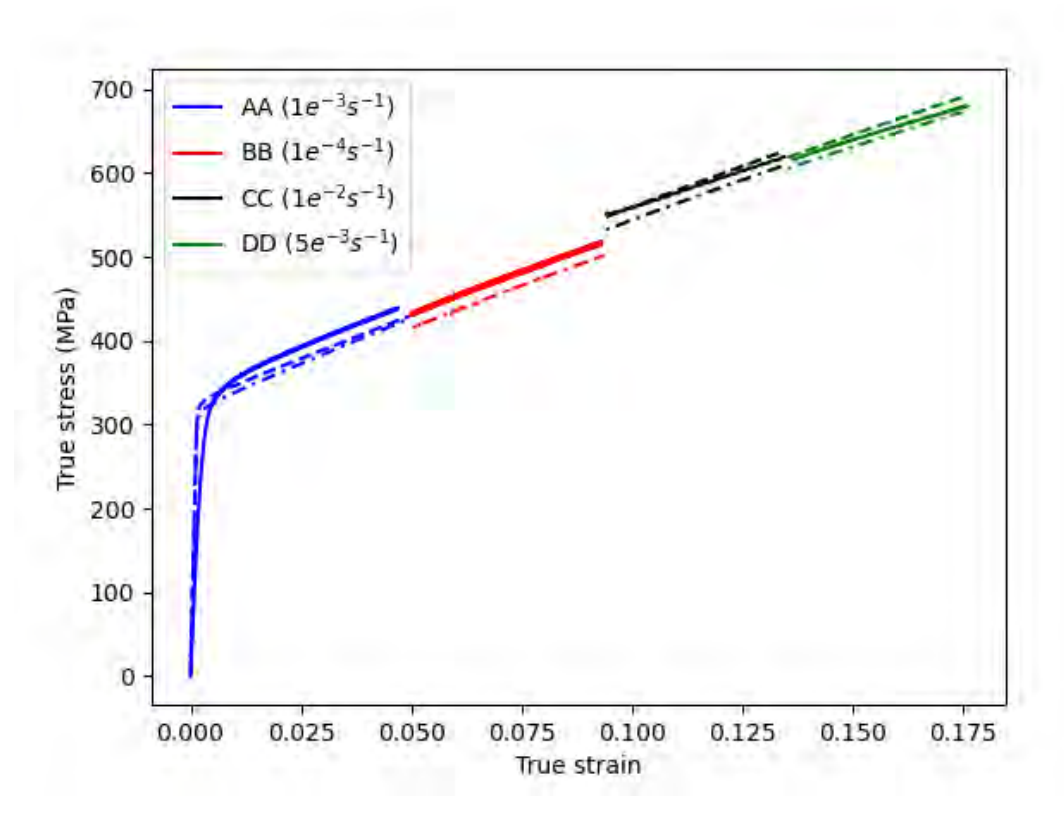


Figure 18: Comparison between experimental and simulated curves from Figure 6 and simulated optimum 2 (dash-dotted) curves with four jumps in strain rate at 20 °C.

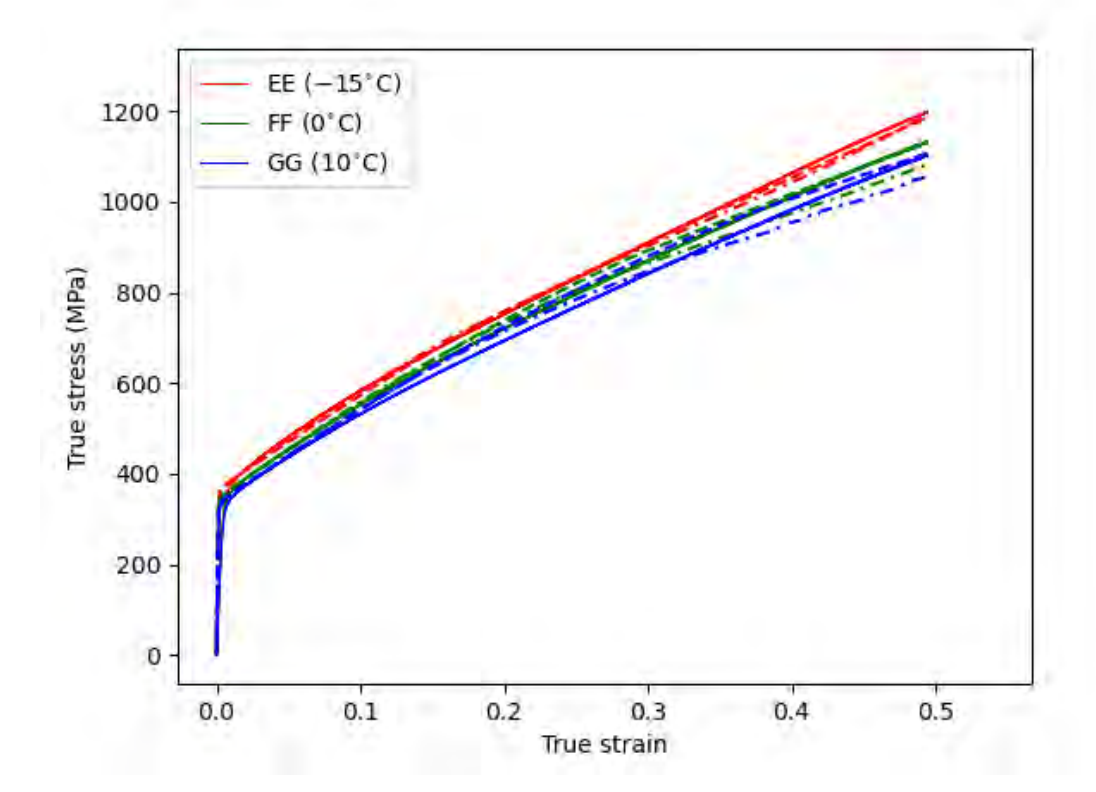


Figure 19: Comparison between experimental and simulated curves from Figure 7 and simulated optimum 2 (dash-dotted) at four temperatures under a strain rate of  $0.001\ s^{-1}$ .

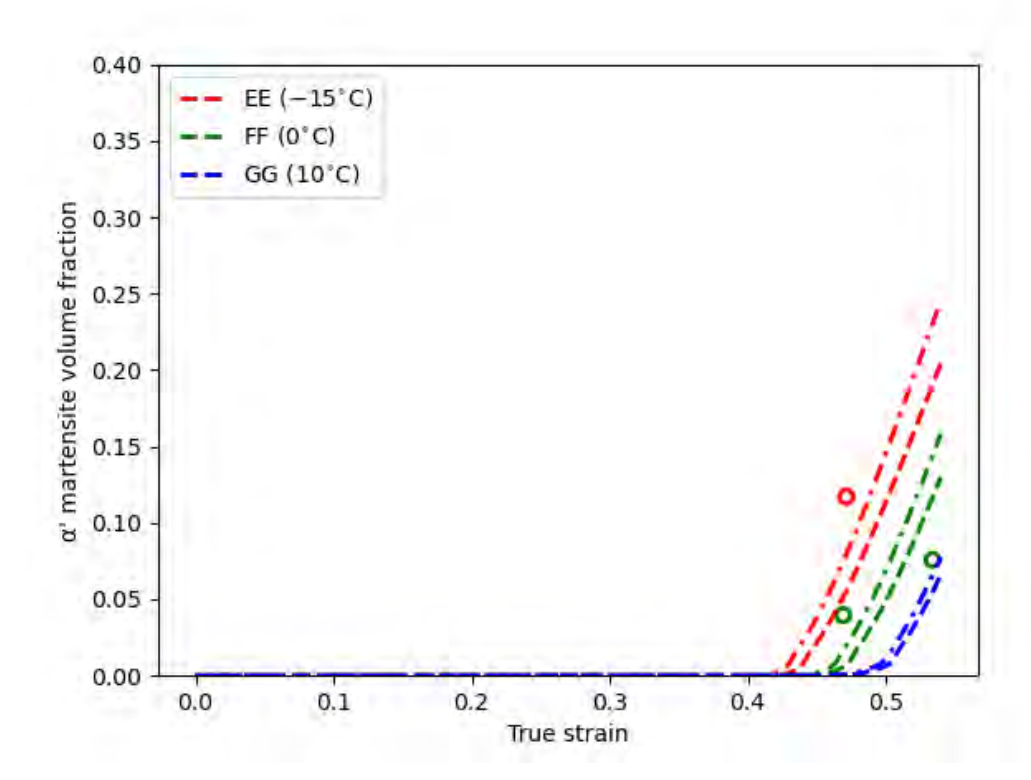


Figure 20: Comparison between experimental and simulated curves from Figure 8 and simulated optimum 2 (dash-dotted) curves showing fraction of  $\alpha'$ -martensite at four temperatures under a constant strain rate. The fraction of  $\varepsilon$ -martensite is nearly zero.

Table 6: Optimum 2 EPSC model parameters for austenite and two martensite phases of SS316L steel.

Parameters	$\gamma$ -Austenite	$\varepsilon ext{-Martensite}$	$\alpha'$ -Martensite
$\kappa_1^{\alpha}[m^{-1}]$	1.34e + 08	0.205e + 08*	2.87e+08
$g^{lpha}$	0.147	1.0e+06*	0.312
$D^{\alpha}[MPa]$	120	100*	326.2
$\tau_{0,a}[MPa]$	385.2	800.0*	325.2
$ au_{0,b}$	0.016	-	-
$ au_{0,c}[K]$	208.9	-	-

# Phase transformation parameters

$m_{SFE}[\frac{mJ}{Km^{-2}}]$	0.1277	$C_{SFE}[\frac{mJ}{m^{-2}}]$	11.5295
$\kappa_{eta}$	0.1187	$eta_0$	0.0781

# D Appendix D: GA versus GP sequential infilling

This appendix presents comparisons between past results from the genetic algorithm optimization and current results obtained using the optimization developed in the present work (Figure 21).

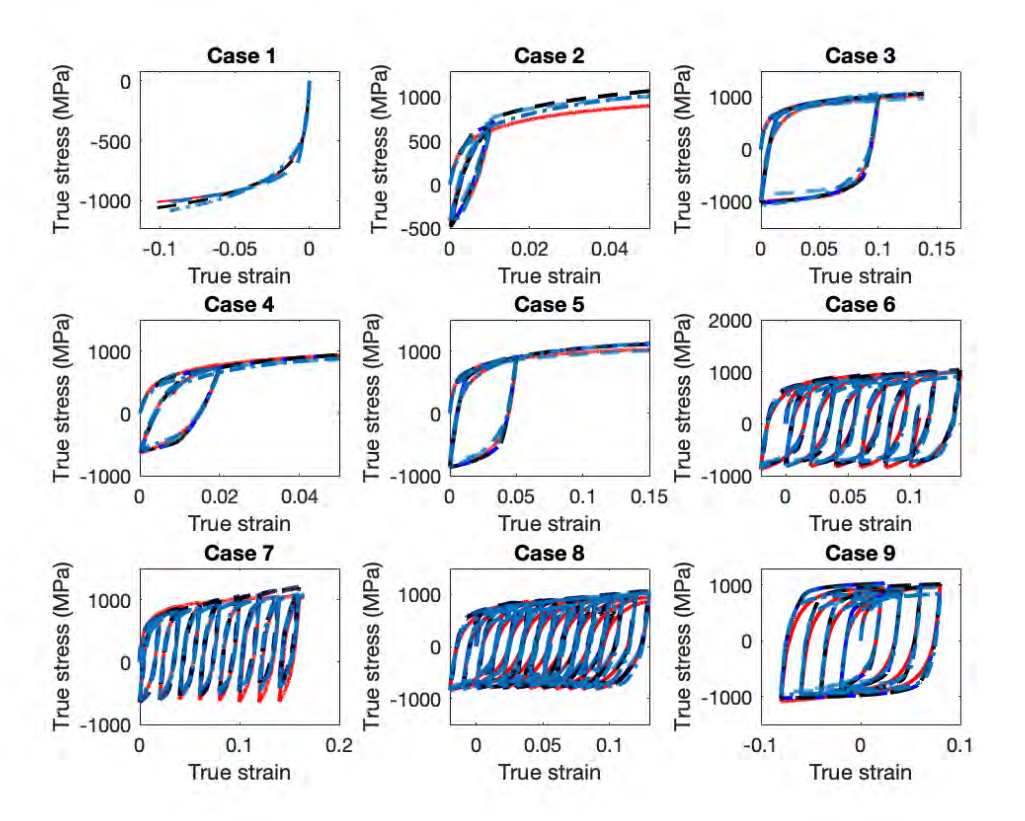


Figure 21: Comparison between experimental curves taken from [49] (solid red lines as in Figures 4 and 5), simulated curves based on the optimum 1 and optimum 2 parameters (blue lines as in Figures 4 and 5), and simulated curves from [32] (dashed black lines).

# References

- [1] Eshelby, J. D., 1957. The determination of the elastic field of an ellipsoidal inclusion, and related problems. Proceedings of the Royal Society of London, Volume 241, Pages 376–396.
- [2] Bathe, K.-J., 1996. Finite element procedures, Englewood Cliffs, N.J.: Prentice Hall.
- [3] Peeters, B., Kalidindi, S. R., Van Houtte, P., Aernoudt, E., 2000. A crystal plasticity based work-hardening/softening model for b.c.c. metals under changing strain paths. Acta Materialia, Volume 48, Pages 2123–2133.
- [4] Knezevic, M., Mccabe, R. J., Tomé, C. N., Lebensohn, R. A., Chen, S. R., Cady, C. M., Gray, G. T., III, & Mihaila, B., 2013. Modeling mechanical response and texture evolution of alpha-uranium as a function of strain rate and temperature using polycrystal plasticity. International Journal of Plasticity, Volume 43, Pages 70–84.
- [5] Daroju, S., Kuwabara, T., Sharma, R., Fullwood, D.T., Miles, M.P., Knezevic, M., 2022. Experimental characterization and crystal plasticity modeling for predicting load reversals in AA6016-T4 and AA7021-T79. International Journal of Plasticity, Volume 153, Pages 103292.
- [6] Knezevic, M., Beyerlein, I.J., Brown, D.W., Sisneros, T.A., Tomé, C.N., 2013. A polycrystal plasticity model for predicting mechanical response and texture evolution during strain-path changes: Application to beryllium. Int. J. Plast. Volume 49, Pages 185-198.
- [7] Ardeljan, M., Savage, D. J., Kumar, A., Beyerlein, I. J., Knezevic, M., 2016. The plasticity of highly oriented nano-layered Zr/Nb composites. Acta. Mater., Volume 115, Pages 189–203.
- [8] Savage, D. J., Beyerlein, I. J., Mara, N. A., Vogel, S. C., McCabe, R. J., Knezevic, M., 2020. Microstructure and texture evolution in Mg/Nb layered materials made by accumulative roll bonding. International Journal of Plasticity, Volume 125, Pages 1–26.
- [9] Zecevic, M., Upadhyay, M. V., Polatidis, E., Panzner, T., Van Swygenhoven, H., Knezevic, M., 2019. A crystallographic extension to the Olson-Cohen model for predicting strain path dependence of martensitic transformation. Acta. Acta. Mater, Volume 166, Pages 386–401.
- [10] Ardeljan, M., McCabe, R.J., Beyerlein, I.J., Knezevic, M., 2015. Explicit incorporation of deformation twins into crystal plasticity finite element models. Computer Methods in Applied Mechanics and Engineering, Volume 295, Pages 396-413.
- [11] Gong, J., Wilkinson, A. J., 2009. Anisotropy in the plastic flow properties of single-crystal alpha titanium determined from micro-cantilever beams. Acta Materialia, Volume 57, Pages 5693–5705.
- [12] Patel, D. K., Kalidindi, S. R., 2017. Estimating the slip resistance from spherical nanoindentation and orientation measurements in polycrystalline samples of cubic metals. International Journal of Plasticity, Volume 92, Pages 19–30.
- [13] Ferreri, N.C., Feng, Z., Savage, D.J., Brown, D.W., Clausen, B., Sisneros, T.A., Knezevic, M., 2022. In-situ high-energy X-ray diffraction and crystal plasticity modeling to predict the evolution of texture, twinning, lattice strains and strength during loading and reloading of beryllium. Int. J. Plast. Volume 150, Pages 103217.

- [14] Benafan, O., Noebe, R. D., Padula, S. A., II, Brown, D. W., Vogel, S., Vaidyanathan, R., 2014. Thermomechanical cycling of a NiTi shape memory alloy-macroscopic response and microstructural evolution. International Journal of Plasticity, Volume 56, Pages 99–118.
- [15] Savage, D. J., McWilliams, B. A., Vogel, S. C., Trujillo, C. P., Beyerlein, I. J., Knezevic, M., 2020. Mechanical behavior and texture evolution of WE43 magnesium-rare earth alloy in Split-Hopkinson Pressure Bar and Taylor Impact Cylinder Testing. International Journal of Impact Engineering, Volume 143, Pages 103589.
- [16] Wehrenberg, C. E., McGonegle, D., Bolme, C., Higginbotham, A., Lazicki, A., Lee, H. J., Nagler, B., Park, H.-S., Remington, B.A., Rudd, R.E., Sliwa, M., Suggit, M., Swift, D., Tavella, F., Zepeda-Ruiz, L., Wark, J. S., 2017. In situ X-ray diffraction measurement of shock-wave-driven twinning and lattice dynamics. Nature, Volume 550, Pages 496–499.
- [17] Zecevic, M., Knezevic, M., Beyerlein, I.J., McCabe, R.J., 2016. Texture formation in orthorhombic alpha-uranium under simple compression and rolling to high strains. Journal of Nuclear Materials, Volume 473, Pages 143-156.
- [18] Mandal, S., T. Gockel, B., Rollett, A. D., 2017. Application of canonical correlation analysis to a sensitivity study of constitutive model parameter fitting. Materials & design, Volume 132, Pages 30–43.
- [19] Savage, D.J., Knezevic, M., 2015. Computer implementations of iterative and non-iterative crystal plasticity solvers on high performance graphics hardware. Computational Mechanics, Volume 56, Pages 677–690.
- [20] Feng, Z., Zecevic, M., Knezevic, M., Lebensohn, R.A., 2022. Predicting extreme anisotropy and shape variations in impact testing of tantalum single crystals. International Journal of Solids and Structures, Volume 241, Pages 111466.
- [21] Walters, D. J., Biswas, A., Lawrence, E. C., Francom, D. C., Luscher, D. J., Fredenburg, D. A., Moran, K.R., Sweeney, C.M., Sandberg, R.L., Ahrens, J.P., Bolme, C. A., 2018. Bayesian calibration of strength parameters using hydrocode simulations of symmetric impact shock experiments of Al-5083. Journal of Applied Physics, Volume 124, Pages 205105.
- [22] Sharma, R., Sargeant, D., Daroju, S., Knezevic, M., Miles, M.P., Fullwood, D.T., 2022. Multi-strain path deformation behavior of AA6016-T4: Experiments and crystal plasticity modeling. International Journal of Solids and Structures, Volume 244-245, Pages 111536.
- [23] Herrera-Solaz, V., LLorca, J., Dogan, E., Karaman, I., Segurado, J., 2014. An inverse optimization strategy to determine single crystal mechanical behavior from polycrystal tests: Application to AZ31 Mg alloy. International Journal of Plasticity, Volume 57, Pages 1–15.
- [24] Dawson, P.R., Boyce, D.E., Park, J-S., Wielewski, E., Miller, M.P., 2018. Determining the strengths of HCP slip systems using harmonic analyses of lattice strain distributions. Acta Materialia, Volume 144, Pages 92-106.
- [25] Wielewski, E., Boyce, D.E., Park, J-S., Miller, M.P., Dawson, P.R., 2017. A methodology to determine the elastic moduli of crystals by matching experimental and simulated lattice strain pole figures using discrete harmonics. Acta Materialia, Volume 126, Pages 469-480.

- [26] Bandyopadhyay, R., Prithivirajan, V., Sangid, M.D., 2019. Uncertainty Quantification in the Mechanical Response of Crystal Plasticity Simulations. JOM Volume 71, Pages 2612–2624.
- [27] Saha, S., Kafka, O.L., Lu, Y. et al., 2021. Microscale Structure to Property Prediction for Additively Manufactured IN625 through Advanced Material Model Parameter Identification. Integr. Mater. Manuf. Innov. Volume 10, Pages 142–156.
- [28] Schowtjak, A., Schulte, R., Clausmeyer, T., Ostwald, R., Tekkaya, E., Menzel, A., 2022. ADAPT A Diversely Applicable Parameter Identification Tool: Overview and full-field application examples. International Journal of Mechanical Sciences, Volume 213, Pages 106840.
- [29] Penuelas, I., Cuesta, I.I., Betegon, C., Rodriguez, C., Belzunce, F.J., 2009. Inverse determination of the elastoplastic and damage parameters on small punch tests. Fatigue & Fracture of Engineering Materials & Structures, Volume 32, Pages 872-885.
- [30] Sun, Q., Lu, Y., Chen J., 2020. Identification of material parameters of a shear modified GTN damage model by small punch test. International Journal of Fracture, Volume 222, Pages 25–35.
- [31] Sedighiani, K., Diehl, M., Traka, K., Roters, F., Sietsma, J., Raabe, D., 2020. An efficient and robust approach to determine material parameters of crystal plasticity constitutive laws from macro-scale stress-strain curves. International Journal of Plasticity, Volume 134, Pages 102779.
- [32] Savage, D. J., Feng, Z., Knezevic, M., 2021. Identification of crystal plasticity model parameters by multi-objective optimization integrating microstructural evolution and mechanical data. Computer Methods in Applied Mechanics and Engineering, Volume 379, Pages 113747.
- [33] Barton, N.R., Knap, J., Arsenlis, A., Becker, R., Hornung, R.D. Jefferson, D.R., 2008. Embedded polycrystal plasticity and adaptive sampling. International Journal of Plasticity, Volume 24, Pages 242-266.
- [34] Schmidt, J., Marques, M.R., Botti, S. and Marques, M.A., 2019. Recent advances and applications of machine learning in solid-state materials science. npj Computational Materials, Volume 5, Pages 1-36.
- [35] Yuan, M., Paradiso, S., Meredig, B., Niezgoda, S.R. 2018. Machine Learning–Based Reduce Order Crystal Plasticity Modeling for ICME Applications. Integrating Materials and Manufacturing Innovation, Volume 7, Pages 214–230.
- [36] Weber, G., Pinz, M., Ghosh, S., 2020. Machine Learning-Aided Parametrically Homogenized Crystal Plasticity Model (PHCPM) for Single Crystal Ni-Based Superalloys. JOM, Volume 72, Pages 4404–4419.
- [37] Mangal, A., Holm, E.A., 2018. Applied machine learning to predict stress hotspots I: Face centered cubic materials. International Journal of Plasticity, Volume 111, Pages 122-134.
- [38] Jung, J., Yoon, J. I., Park, H. K., Kim, J. Y., Kim, H. S., 2019. An efficient machine learning approach to establish structure-property linkages. Computational Materials Science, Volume 156, Pages 17–25.
- [39] Mastrippolito, F., Aubert, S. Ducros, F., 2021. Kriging metamodels-based multi-objective shape optimization applied to a multi-scale heat exchanger. Computers & Fluids, Volume 221, Pages 104899.

- [40] Sacks, J., Welch, W. J., Mitchell, T. J., Wynn, H. P., 1989. Design and Analysis of Computer Experiments. Statistical science: a review journal of the Institute of Mathematical Statistics, Volume 4, Pages 409–423.
- [41] Rasmussen, C. E., & Williams, C. K. I. 2005. Gaussian processes for machine learning. MIT Press.
- [42] Jones, D. R., Schonlau, M., Welch, W. J., 1998. Efficient Global Optimization of Expensive Black-Box Functions. Journal of Global optimization, Volume 13, Pages 455–492.
- [43] Rojas-Gonzalez, S., Van Nieuwenhuyse, I., 2020. A survey on kriging-based infill algorithms for multiobjective simulation optimization. Computers & Operations Research, Volume 116, Pages 104869.
- [44] Binois, M., Picheny, V., 2019. GPareto: An R Package for Gaussian-Process-Based Multi-Objective Optimization and Analysis. Journal of Statistical Software, Volume 89, Pages 1–30.
- [45] Álvarez, M. A., Rosasco, L., Lawrence, N. D., 2012. Kernels for vector-valued functions: A review. Foundations and Trends in Machine Learning, Volume 4, Pages 195–266.
- [46] Ponweiser, W., Wagner, T., Biermann, D., Vincze, M., 2008. Multiobjective Optimization on a Limited Budget of Evaluations Using Model-Assisted S-Metric Selection. In G Rudolph, et al. (eds.), PPSN X Volume 5199, Pages 784–794. Springer-Verlag.
- [47] Guerreiro, A. P., Fonseca, C. M., & Paquete, L. (2021). The Hypervolume Indicator: Computational Problems and Algorithms. ACM Comput. Surv., Volume 54. Pages 3453474.
- [48] Whitley, D. (1994). A genetic algorithm tutorial. Statistics and computing, Volume 4, Pages 65–85.
- [49] Daroju, S., Kuwabara, T., Knezevic, M., 2022. Experimental characterization and crystal plasticity modeling of dual-phase steels subjected to strain path reversals. Mechanics of Materials: An International Journal, Volume 168, Pages 104293.
- [50] Eghtesad, A., Barrett, T.J., Knezevic, M., 2018. Compact reconstruction of orientation distributions using generalized spherical harmonics to advance large-scale crystal plasticity modeling: Verification using cubic, hexagonal, and orthorhombic polycrystals. Acta. Mater. Volume 155, Pages 418-432.
- [51] Knezevic, M., Landry, N.W., 2015. Procedures for reducing large datasets of crystal orientations using generalized spherical harmonics. Mechanics of Materials, Volume 88, Pages 73-86.
- [52] Barrett, T.J., Eghtesad, A., McCabe, R.J., Clausen, B., Brown, D.W., Vogel, S.C., Knezevic, M., 2019. A generalized spherical harmonics-based procedure for the interpolation of partial datasets of orientation distributions to enable crystal mechanics-based simulations. Materialia Volume 6, Pages 100328.
- [53] Feng, Z., Mamros, E.M., Ha, J., Kinsey, B.L., Knezevic, M., 2021. Modeling of plasticity-induced martensitic transformation to achieve hierarchical, heterogeneous, and tailored microstructures in stainless steels. CIRP Journal of Manufacturing Science and Technology, Volume 33, Pages 389-397.

- [54] Mamros, E.M., Kuijer, B.M., Davarpanah, M.A., Baker, I., Kinsey, B.L., 2021. The Effect of Temperature on the Strain-Induced Austenite to Martensite Transformation in SS 316L During Uniaxial Tension. In: Daehn, G., Cao, J., Kinsey, B., Tekkaya, E., Vivek, A., Yoshida, Y. (eds) Forming the Future. The Minerals, Metals and Materials Series. Springer, Cham.
- [55] Mamros, E.M., Eaton, M.C., Ha, J., Kinsey, B.L., 2021. Numerical Analysis of SS316L Biaxial Cruciform Specimens Under Proportional Loading Paths. Proceedings of the ASME 2021 16th International Manufacturing Science and Engineering Conference. Volume 2: Manufacturing Processes; Manufacturing Systems; Nano/Micro/Meso Manufacturing; Quality and Reliability.
- [56] Dupuy, D., Helbert, C., & Franco, J., 2015. DiceDesign and DiceEval: Two R Packages for Design and Analysis of Computer Experiments. Journal of Statistical Software, Volume 65, Pages 1–38.
- [57] Knezevic, M., Al-Harbi, H.F., Kalidindi, S.R., 2009. Crystal plasticity simulations using discrete Fourier transforms. Acta Materialia, Volume 57, Pages 1777-1784.
- [58] Al-Harbi, H.F., Knezevic, M., Kalidindi, S.R., 2010. Spectral approaches for the fast computation of yield surfaces and first-order plastic property closures for polycrystalline materials with cubic-triclinic textures. Computers, Materials, Continua, Volume 15, Pages 153-172.
- [59] Knezevic, M., Kalidindi, S.R., Fullwood, D., 2008. Computationally efficient database and spectral interpolation for fully plastic Taylor-type crystal plasticity calculations of face-centered cubic polycrystals. Int. J. Plast., Volume 24, Pages 1264-1276.
- [60] Ardeljan, M., Beyerlein, I.J., McWilliams, B.A., Knezevic, M., 2016. Strain rate and temperature sensitive multi-level crystal plasticity model for large plastic deformation behavior: Application to AZ31 magnesium alloy. International Journal of Plasticity, Volume 83, Pages 90-109.
- [61] Kalidindi, S.R., Bronkhorst, C.A., Anand, L., 1992. Crystallographic texture evolution in bulk deformation processing of FCC metals. Journal of the Mechanics and Physics of Solids, Volume 40, Pages 537-569.
- [62] Feather, W.G., Ghorbanpour, S., Savage, D.J., Ardeljan, M., Jahedi, M., McWilliams, B.A., Gupta, N., Xiang, C., Vogel, S.C., Knezevic, M., 2019. Mechanical response, twinning, and texture evolution of WE43 magnesium-rare earth alloy as a function of strain rate: Experiments and multi-level crystal plasticity modeling. Int. J. Plast., Volume 120, Pages 180-204.
- [63] Feather, W.G., Lim, H., Knezevic, M., 2021. A numerical study into element type and mesh resolution for crystal plasticity finite element modeling of explicit grain structures, Comput. Mech., Volume 67, Pages 33-55.
- [64] Feather, W.G., Savage, D.J., Knezevic, M., 2021. A crystal plasticity finite element model embedding strain-rate sensitivities inherent to deformation mechanisms: Application to alloy AZ31. Int. J. Plast., Volume 143, Pages 103031.
- [65] Lebensohn, R.A., Tomé, C.N., 1993. A self-consistent anisotropic approach for the simulation of plastic deformation and texture development of polycrystals: Application to zirconium alloys. Acta Metallurgica et Materialia, Volume 41, Pages 2611-2624.

- [66] Marki, R.E., Brindley, K.A., McCabe, R.J., Knezevic, M., 2022. Crystal mechanics-based thermo-elastic constitutive modeling of orthorhombic uranium using generalized spherical harmonics and first-order bounding theories. Journal of Nuclear Materials, Volume 560, Pages 153472.
- [67] Zecevic, M., Beyerlein, I.J., Knezevic, M., 2017. Coupling elasto-plastic self-consistent crystal plasticity and implicit finite elements: Applications to compression, cyclic tension-compression, and bending to large strains. International Journal of Plasticity, Volume 93, Pages 187-211.
- [68] Barrett, T.J., Knezevic, M., 2019. Deep drawing simulations using the finite element method embedding a multi-level crystal plasticity constitutive law: Experimental verification and sensitivity analysis. Computer Methods in Applied Mechanics and Engineering, Volume 354, Pages 245-270.
- [69] Eghtesad, A., Germaschewski, K., Lebensohn, R.A., Knezevic, M., 2020. A multi-GPU implementation of a full-field crystal plasticity solver for efficient modeling of high-resolution microstructures. Computer Physics Communications, Volume 254, Pages 107231.
- [70] Eghtesad, A., Barrett, T.J., Germaschewski, K., Lebensohn, R.A., Mc-Cabe, R.J., Knezevic, M., 2018. OpenMP and MPI implementations of an elasto-viscoplastic fast Fourier transform-based micromechanical solver for fast crystal plasticity modeling. Advances in Engineering Software, Volume 126, Pages 46-60.
- [71] Eghtesad, A., Germaschewski, K., Knezevic, M., 2022. Coupling of a multi-GPU accelerated elasto-visco-plastic fast Fourier transform constitutive model with the implicit finite element method. Comput. Mater. Sci., Volume 208, Pages 111348.
- [72] Eghtesad, A., Knezevic, M., 2020. High-performance full-field crystal plasticity with dislocation-based hardening and slip system back-stress laws: Application to modeling deformation of dual-phase steels, J. Mech. Phys. Solids, Volume 134, Pages 103750.
- [73] Cantara, A.M., Zecevic, M., Eghtesad, A., Poulin, C.M., Knezevic, M., 2019. Predicting elastic anisotropy of dual-phase steels based on crystal mechanics and microstructure. Int. J. Mech. Sci. Volume 151, Pages 639–649.
- [74] Knezevic, M., Kalidindi, S.R., 2007. Fast computation of first-order elastic-plastic closures for polycrystalline cubic-orthorhombic microstructures. Comput. Mater. Sci. Volume 39, Pages 643-648.
- [75] Feng, Z., Zecevic, M., Knezevic, M., 2021. Stress-assisted  $(\gamma \rightarrow \alpha')$  and strain-induced  $(\gamma \rightarrow \varepsilon \rightarrow \alpha')$  phase transformation kinetics laws implemented in a crystal plasticity model for predicting strain path sensitive deformation of austenitic steels. International Journal of Plasticity, Volume 136, 102807.
- [76] Zecevic, M., Pantleon, W., Lebensohn, R.A., McCabe, R.J., Knezevic, M., 2017. Predicting intragranular misorientation distributions in polycrystalline metals using the viscoplastic self-consistent formulation. Acta Materialia, Volume 140, Pages 398-410.
- [77] Zecevic, M., Lebensohn, R.A., McCabe, R.J., Knezevic, M., 2018. Modeling of intragranular misorientation and grain fragmentation in polycrystalline materials using the viscoplastic self-consistent formulation. International Journal of Plasticity, Volume 109, Pages 193-211.

- [78] Lebensohn, R.A., Zecevic, M., Knezevic, M., McCabe, R.J., 2016. Average intragranular misorientation trends in polycrystalline materials predicted by a viscoplastic self-consistent approach. Acta Materialia, Volume 104, Pages 228-236.
- [79] Zecevic, M., Knezevic, M., McWilliams, B., Lebensohn, R.A., 2020. Modeling of the thermo-mechanical response and texture evolution of WE43 Mg alloy in the dynamic recrystallization regime using a viscoplastic self-consistent formulation. Int. J. Plast., Volume 130, Pages 102705.
- [80] Zecevic, M., Lebensohn, R.A., McCabe, R.J., Knezevic, M., 2019. Modelling recrystallization textures driven by intragranular fluctuations implemented in the viscoplastic self-consistent formulation. Acta. Mater., Volume 164, Pages 530-546.
- [81] Wang, H., Jeong, Y., Clausen, B., Liu, Y., McCabe, R.J., Barlat, F., Tomé, C.N., 2016. Effect of martensitic phase transformation on the behavior of 304 austenitic stainless steel under tension. Materials Science and Engineering: A, Volume 649, Pages 174-183.
- [82] Landry, N., Knezevic, M., 2015. Delineation of First-Order Elastic Property Closures for Hexagonal Metals Using Fast Fourier Transforms. Materials Volume 8, Pages 6326-6345.
- [83] Zecevic, M., Knezevic, M., 2019. An implicit formulation of the elasto-plastic self-consistent polycrystal plasticity model and its implementation in implicit finite elements. Mechanics of Materials, Volume 136, Pages 103065.
- [84] Beyerlein, I.J., Tomé, C.N., 2008. A dislocation-based constitutive law for pure Zr including temperature effects. International Journal of Plasticity, Volume 24, Pages 867-895.
- [85] Zecevic, M., Knezevic, M., 2017. Modeling of Sheet Metal Forming Based on Implicit Embedding of the Elasto-Plastic Self-Consistent Formulation in Shell Elements: Application to Cup Drawing of AA6022-T4. JOM, Volume 69, Pages 922-929.
- [86] Zecevic, M., Korkolis, Y.P., Kuwabara, T., Knezevic, M., 2016. Dual-phase steel sheets under cyclic tension–compression to large strains: Experiments and crystal plasticity modeling. Journal of the Mechanics and Physics of Solids, Volume 96, Pages 65-87.
- [87] Turner, P.A., Tomé, C.N., 1994. A study of residual stresses in Zircaloy-2 with rod texture. Acta Metallurgica et Materialia. Volume 42, Pages 4143-4153.
- [88] Zecevic, M., Knezevic, M., 2018. Latent hardening within the elastoplastic self-consistent polycrystal homogenization to enable the prediction of anisotropy of AA6022-T4 sheets. International Journal of Plasticity, Volume 105, Pages 141-163.
- [89] Knockaert, R., Chastel, Y., Massoni, E., 2000. Rate-independent crystalline and polycrystalline plasticity, application to FCC materials. International Journal of Plasticity, Volume 16, Pages 179-198.
- [90] Franciosi, P., Zaoui, A., 1982. Multislip in f.c.c. crystals a theoretical approach compared with experimental data. Acta Metallurgica, Volume 30, Pages 1627-1637.
- [91] Khadyko, M., Dumoulin, S., Cailletaud, G., Hopperstad, O.S., 2016. Latent hardening and plastic anisotropy evolution in AA6060 aluminium alloy. International Journal of Plasticity, Volume 76, Pages 51-74.

- [92] Olson, G.B., Cohen, M., 1976. A general mechanism of martensitic nucleation: Part I. General concepts and the FCC  $\rightarrow$  HCP transformation. Metallurgical and Material Transactions: A, Volume 7, Pages 1897–1904
- [93] Cahn, R.W., Haasen, P., 1996. Physical Metallurgy. ISBN: 9780080538945
- [94] Bhadeshia, H.K.D.H., 2001. Worked Examples in the Geometry of Crystals. The Institute of Metals North American Publications Center.
- [95] Christian, J.W., Mahajan, S., 1995. Deformation twinning. Progress in Materials Science, Volume 39, Pages 1-157.
- [96] Ericsson, T., 1966. The temperature and concentration dependence of the stacking fault energy in the Co-Ni system. Acta Metallurgica, Volume 14, Pages 853-865.
- [97] Latanision, R.M., Ruff, A.W., 1971. The temperature dependence of stacking fault energy in Fe-Cr-Ni alloys. Metallurgical and Material Transactions: B Volume 2, Pages 505–509.